

AN UNSPLIT STAGGERED MESH SCHEME FOR MULTIDIMENSIONAL MAGNETOHYDRODYNAMICS WITH EFFICIENT DISSIPATION CONTROLS

Dongwook Lee^a and Anil Deane^{b,*}

^a*ASC FLASH Center, University of Chicago, 5640 S. Ellis, Chicago, IL 60637*

^b*Institute for Physical Science and Technology, University of Maryland, College Park, MD 20742*

– PREPRINT –

November 5, 2007

Abstract

We introduce an unsplit staggered mesh scheme (USM) that solves multidimensional magnetohydrodynamics (MHD) by a constrained transport method with high-order Godunov fluxes, incorporating three new developments that enhance performance. The USM scheme handles multidimensional MHD terms, proportional to $\nabla \cdot \mathbf{B}$, in a new directionally unsplit data reconstruction step. This reconstruction step maintains in-plane dynamics very well, as shown by two-dimensional tests. The scheme uses a compact form of the discrete induction equation and since the accuracy of the computed electric field directly influences the quality of the magnetic field solution, we address the lack of proper dissipative behavior in previous electric field averaging schemes and present a new modified electric field construction (MEC) that includes multidimensional derivative information and is more accurate. We also obtain a relation between the induction equation and its difference form and use this to derive a set of corresponding modified equations which show anti-dissipative behavior of cell-face magnetic fields. We present an efficient treatment suppressing the anti-dissipative terms by introducing a difference formulation with balancing dissipation control (DC) that maintains the divergence-free property on a staggered meshes. We use this difference scheme to highlight important properties that avoid unphysical growth of field variables. Our numerical tests show that numerical instability can occur if the anti-dissipation terms are ignored or otherwise not explicitly controlled. A series of comparison studies demonstrates the excellent performance of the full USM-MEC-DC scheme for many quite stringent multidimensional MHD test problems. The scheme is implemented and currently available in the University of Chicago ASC FLASH Center’s FLASH 3 release.

1 Introduction

A well-designed numerical MHD algorithm should generate solutions that reflect the fact that there are no isolated magnetic monopoles. Brackbill and Barnes (1980) [6] showed that violating the $\nabla \cdot \mathbf{B} = 0$ constraint can cause fictitious forces to develop parallel to the magnetic fields. This can result in extra source terms in the momentum, induction and energy equations. For instance, the Lorentz force per unit volume (assuming overall charge neutrality) can be written as

$$\mathbf{j} \times \mathbf{B} = (\nabla \times \mathbf{B}) \times \mathbf{B} \quad (1)$$

*Corresponding author, deane@ipst.umd.edu.

$$= (\mathbf{B} \cdot \nabla) \mathbf{B} - \frac{1}{2} \nabla B^2 \quad (2)$$

$$= \nabla \cdot (\mathbf{B}\mathbf{B}) - (\nabla \cdot \mathbf{B}) \mathbf{B} - \frac{1}{2} \nabla B^2, \quad (3)$$

where \mathbf{j} and B are the current density and magnitude of the magnetic fields. The first and second terms in equation (2) represent the forces from magnetic tension and magnetic pressure, respectively.

From (3), if $\nabla \cdot \mathbf{B} \neq 0$ the nonzero value of $\nabla \cdot \mathbf{B}$ will grow proportionally with \mathbf{B} producing an extra compressive magnetic component parallel to the magnetic field and an unphysical magnetic acceleration along the field lines. Since the gas pressure,

$$p = (\gamma - 1) \left(E - \frac{1}{2} \rho U^2 - \frac{1}{2} B^2 \right), \quad (4)$$

where E, U , and B are the total energy density, magnitudes of velocity fields and magnetic fields respectively, in simulations, nonzero $\nabla \cdot \mathbf{B}$ value will increase the magnetic pressure $\frac{1}{2} B^2$ and from (4), the gas pressure p will correspondingly be reduced relative to the divergence-free case. In many numerical simulations, $\nabla \cdot \mathbf{B}$ is typically small, but not exactly zero, and being a discretization error, the resultant error can accumulate over the computational domain and produce erroneous solutions.

More generally, unphysical growth of the magnetic field in a simulation can lead to negative pressure states in very low β plasma flows in a region where a predictive magnetic pressure exhibits spurious growth rates, which in turn, fails to preserve the physical positivity of gas pressure. On the other hand in very high β regimes it is also hard to maintain correct plasma flow properties because very weak magnetic fields can easily be affected at the level of discretization errors. In either case, erroneous magnetic field growth rates influence the energy balance between the thermal and magnetic pressures, potentially changing the topology of the magnetic fields, affecting the global field configuration and attendant particle propagation.

For these reasons attention has been paid to staggered mesh schemes which naturally avoid these issues. Here we develop a new such discrete formulation for the induction equation which avoids unphysical growth of the magnetic fields, and produces accurate and stable plasma solutions over a wide range of plasma β .

1.1 Cell-centered Fields Algorithms in High-Order Godunov MHD

Over the last decade high-order Godunov methods, originally developed in hydrodynamics, have become of great interest in MHD because of their accuracy and robustness. A brief list of developments includes the work of Brio and Wu (1988) [8], Zachary, Malagoli, and Colella (1994) [37], Dai and Woodward (1994) [11], Powell *et al.* (1994) [28], Ryu and Jones (1995) [30], Balsara and Spicer (1998) [2], Londrillo and Del Zanna (1999) [24], Pen *et al.* (2003) [27], Londrillo and Del Zanna (2004) [25], Balsara (2003) [4], Crockett *et al.* (2005) [10], and Gardiner and Stone (2005) [17].

The high-order Godunov scheme, first developed by van Leer (1979) for Euler flows has thereafter opened a new era of robust and accurate performance in numerical simulations of MHD as well as hydrodynamics. Early efforts in high-order Godunov MHD schemes focused entirely on numerical formulations that collocated the magnetic fields at cell centers because the underlying aspects of Godunov algorithms are based on conservation laws in which the cell-centered variables are conserved. Thus the MHD equations were treated as a straightforward system of conservation laws in earlier Godunov formulations.

In formulations with cell-centered fields there is no particular difficulty encountered except in multidimensions. This is because in one-dimensional MHD the normal field is held constant and divergence-less evolution of the magnetic fields is obtained naturally. In multidimensional MHD, however, the requirement of maintaining the solenoidal constraint involves solving the induction equation, which for ideal MHD has the form,

$$\frac{\partial \mathbf{B}}{\partial t} + \nabla \times \mathbf{E} = 0. \quad (5)$$

Taking the divergence of the induction equation (5) gives,

$$\frac{\partial \nabla \cdot \mathbf{B}}{\partial t} = \nabla \cdot (-\nabla \times \mathbf{E}) = 0, \quad (6)$$

and we see that the induction equation implies the divergence-less evolution of the magnetic fields. This analytical result may not hold true numerically, because the discrete divergence of the discrete curl may not give zero identically.

Until recently, two traditional approaches have been proposed to enforce the divergence-free constraint in formulations using cell-centered fields. The first is the projection method, proposed by Brackbill and Barnes in the context of MHD[6] (see also early works cited in [1, 30, 37] and recently in [10]), which takes a divergence-cleaning step in their high-order Godunov based MHD scheme. In this approach two choices are available, a scalar or vector divergence-cleaning, depending on the choice of real or Fourier spaces in which the divergence-cleaning is performed. The disadvantage of the approach is the cost of the associated Poisson equation solution by either direct or iterative methods. In addition to the computational expensive, the projection methods has restrictions on types of boundary conditions and associated difficulties on non-Cartesian domains. On a parallel or distributed computer, since the method requires a global solution to a Poisson equation, there is an additional coding burden and cost of all-to-all communication. Yet another disadvantage is extra complexity because the discretization of the elliptic equation must be compatible with that of the MHD equations. An adaptive mesh refinement (AMR) scheme can be implemented in the scalar divergence-cleaning approach, but become progressively computationally expensive as the AMR hierarchy increases in the Poisson solve. The situation is even more acute for implementing a vector divergence-cleaning approach for an AMR algorithm. For more details on these and other numerical issues for this approach see [5, 35].

The second method, the so-called 8-wave formalism, proposed by Powell *et al.* [29], utilizes the modified MHD equations that explicitly includes source terms proportional to $\nabla \cdot \mathbf{B}$. An additional eighth wave reflects the propagation of the magnetic monopole "field," designed to be convected with local flow speeds, and eventually advected out of the computational domain. Although the scheme is found to be robust and accurate (as compared to the basic conservative scheme), this results in a non-conservative form of the MHD governing equations and is susceptible to producing incorrect jump conditions and propagation speeds across discontinuities in certain problems [29, 35]. Because of its inherent formalism allowing a truncation error of $\nabla \cdot \mathbf{B}$ this scheme lacks the divergence-free property and can potentially fail to capture correct magnetic field topologies. There have also been other approaches [13, 20] to extend 8-wave schemes that manifest $\nabla \cdot \mathbf{B}$ as a source term.

1.2 Cell Face-centered Fields Algorithms in High-Order Godunov MHD: the Staggered Mesh Algorithm

To overcome issues raised in formulating high-order Godunov based MHD using cell-centered fields, researchers have developed various staggered mesh algorithms that use a staggered collocation of the magnetic field and solve the induction equation (5) via a discrete form of Stokes' Theorem.

The staggered mesh algorithm, first introduced by Yee (1966) [36] to compute divergence-free MHD flows in a finite difference formulation that transports the electromagnetic fields, has resulted in numerous approaches. Bretcht *et al.* (1981) [7] used a staggered mesh formulation for their global MHD modeling of Earth's magnetosphere for which they used a non-linear FCT flux limiter. Evans and Hawley [15] followed a vector potential approach on a staggered grid for evolution of the MHD induction equation. Another approach by DeVore (1991) [14] also used the staggered mesh arrangement and applied it using a flux corrected transport (FCT) algorithm. Following Evans and Hawley (1988) [15], the term *constrained transport* (CT) has become popular and encompasses all the various methods developed with a staggered mesh approach.

[2, 4, 12, 14, 15, 17, 24, 31, 35]. The original CT method placed the surface variables – the components of the magnetic field – at the cell face centers (cell-faces), and the rest of the volumetric variables such as mass, momentum and energy at the cell-centers on a staggered grid. A variant CT approach by Tóth [35] placed all of the variables at the cell centers and used central differencing for the induction equation. Tóth also made an extensive comparative study of different MHD schemes focusing on the divergence-free property of each scheme. and compared various approaches differing in how the base scheme (*e.g.* van Leer’s TVD-MUSCL, or Yee’s TVD-Lax Friedrich) is modified with regard to the induction equation. Tóth’s study not only compared three major algorithms (*e.g.* projection schemes, 8-wave schemes, and CT based staggered mesh schemes) but also different approaches within the CT formulation.

In CT schemes, different approaches are adopted in obtaining the electric field, $\mathbf{E} = -\mathbf{u} \times \mathbf{B}$ (in ideal MHD). The *flux*-CT scheme of Balsara and Spicer [2] uses second-order Godunov fluxes to construct \mathbf{E} by using the so-called duality relationship between the components of the flux vector and the electric fields. The *field-interpolated* CT scheme of Dai and Woodward [12] uses interpolated magnetic and velocity fields to obtain the electric field in their Godunov-type formulation. Ryu *et al.* [31] also proposed a *transport-flux-interpolated* CT scheme which basically transports the upwind fluxes along with the upwind correction terms for maintaining the TVD property. Balsara studied [3, 4] a new reconstruction algorithm for cell-centered magnetic fields. In this *modified*-CT approach the magnetic fields at each cell center are reconstructed directly from divergence-free cell-face field components using a reconstruction polynomial. By design such reconstructed magnetic fields at the cell centers (and not only the cell-face fields) are also guaranteed to maintain the divergence-free constraint. Recently, Gardiner and Stone [17] have developed a multidimensional CT scheme that is consistent with plane-parallel, grid-aligned one-dimensional base flow problems by modifying the simple arithmetic electric field averaging scheme of Balsara and Spicer [2]. Another approach, *upwinding*-CT (UTC) scheme, was proposed by Londrillo and Del Zanna [25]. Their approach used a similar reconstruction algorithm as in [3, 4] for the magnetic field and evaluates the electric field based on an upwinding strategy in their Godunov-type scheme. In the UTC scheme, the divergence-free property is maintained intrinsically. Yet it is evident from their test results that the scheme suffers from keeping $\nabla \cdot \mathbf{B}$ only approximately low, allowing values up to an order of 10^{-4} (See [24]), while, as shown later the scheme presented here preserves $\nabla \cdot \mathbf{B}$ to the order of $10^{-12} - 10^{-16}$ in simulations. It is worth mentioning that, in Tóth’s work [35], one of the most accurate high-order MHD schemes is the flux-CT scheme of Balsara and Spicer [2]. Balsara [3, 4] has also extended his original flux-CT scheme and implemented it on an AMR grid.

In developing our scheme we adopt the flux-CT approach of [2] and extend its basic ideas to develop a new unsplit staggered mesh scheme. Upon systematically developing a modified electric field construction (MEC) and dissipation control (DC) we term our complete schemes USM-MEC-DC.

The paper is organized as follows. In Section 2, we first introduce a new second-order MUSCL-Hancock type data reconstruction scheme using a single step characteristic tracing formalism. This step includes multidimensional MHD terms important in nonlinear evolutionary plasma flows. The data reconstruction step is followed by solving a Riemann problem that produces high-order Godunov fluxes. Using these fluxes, in Section 3, we present a new modified electric field construction (MEC) algorithm that extends the basic construction scheme of Balsara and Spicer [2] to a scheme containing multidimensional gradient information. In Section 4, we examine a discrete form of the induction equation that has been used in CT-type schemes and its address anti-dissipative properties by studying associated modified equations. We use this relationship to present a new discrete formulation that controls anti-dissipation and also ensures the divergence-free constraint. In Section 5 we present results of various test problems that demonstrate the significant quantitative and qualitative performance of our scheme. We conclude the paper in Section 6.

2 The USM scheme in Ideal MHD

We focus on solving the equations of ideal magnetohydrodynamics (MHD) formulated as hyperbolic system of conservation laws as

$$\frac{\partial \rho}{\partial t} + \nabla \cdot (\rho \mathbf{u}) = 0, \quad (7)$$

$$\frac{\partial \rho \mathbf{u}}{\partial t} + \nabla \cdot (\rho \mathbf{u} \mathbf{u} - \mathbf{B} \mathbf{B}) + \nabla p_{tot} = 0, \quad (8)$$

$$\frac{\partial \mathbf{B}}{\partial t} + \nabla \cdot (\mathbf{u} \mathbf{B} - \mathbf{B} \mathbf{u}) = 0, \quad (9)$$

$$\frac{\partial E}{\partial t} + \nabla \cdot (\mathbf{u} e + \mathbf{u} p_{tot} - \mathbf{B} \mathbf{B} \cdot \mathbf{u}) = 0. \quad (10)$$

The above equations represent the continuity, momentum, induction, and energy equations respectively. The conservative variables include the plasma mass density ρ , momentum $\rho \mathbf{u}$, magnetic field \mathbf{B} , and total energy density E . The plasma velocity is \mathbf{u} , current density $\mathbf{j} = \nabla \times \mathbf{B}$, total pressure $p_{tot} = p + \mathbf{B}^2/2$, and thermal pressure $p = (\gamma - 1)(E - \frac{1}{2}\rho U^2 - \frac{1}{2}\mathbf{B}^2)$, with $U^2 = u^2 + v^2 + w^2$, $B^2 = B_x^2 + B_y^2 + B_z^2$, and γ is ratio of specific specific heats. In addition, the MHD equations should satisfy the solenoidal constraint $\nabla \cdot \mathbf{B} = 0$, which is implicit in the conservation form. The above equations can be written in a matrix form, e.g., in two-dimension,

$$\frac{\partial \mathbf{U}}{\partial t} + \frac{\partial \mathbf{F}}{\partial x} + \frac{\partial \mathbf{G}}{\partial y} = 0, \quad (11)$$

where \mathbf{U} contains the eight MHD conservative variables and \mathbf{F}, \mathbf{G} represent corresponding conservative fluxes in x, y directions. The conserved variable vector

$$\mathbf{U} = (\rho, \rho u, \rho v, \rho w, B_x, B_y, B_z, E)^T, \quad (12)$$

and multidimensional fluxes \mathbf{F}, \mathbf{G} are

$$\mathbf{F} = \begin{pmatrix} \rho u \\ \rho u^2 + p_{tot} - B_x^2 \\ \rho uv - B_y B_x \\ \rho uw - B_z B_x \\ 0 \\ uB_y - vB_x (= -E_z) \\ uB_z - wB_x (= E_y) \\ (E + p_{tot})u - B_x(uB_x + vB_y + wB_z) \end{pmatrix}, \quad (13)$$

$$\mathbf{G} = \begin{pmatrix} \rho v \\ \rho vu - B_x B_y \\ \rho v^2 + p_{tot} - B_y^2 \\ \rho vw - B_z B_y \\ vB_x - uB_y (= E_z) \\ 0 \\ vB_z - wB_y (= -E_x) \\ (E + p_{tot})v - B_y(uB_x + vB_y + wB_z) \end{pmatrix}. \quad (14)$$

Note that Ohm's law for perfectly conducting plasma, $\mathbf{E} = -\mathbf{u} \times \mathbf{B}$, has been used, where $\mathbf{E} \equiv (E_x, E_y, E_z)^T$, is the electric fields.

2.1 Data Reconstruction for High-order Godunov Scheme

The first step of the USM scheme for multidimensional MHD uses a second-order MUSCL-Hancock type TVD algorithm for data reconstruction. The reconstruction uses cell-centered data to calculate cell interface values that are required to solve a Riemann problem. In this reconstruction step it is important to include terms that reflect the multidimensional character of the MHD equations. These relationships have usually been ignored in one-dimension based dimensionally split type data reconstruction formulations but were recently highlighted by Crockett *et al.* [10] and Gardiner *et al.* [17].

In this section we present a new directionally unsplit data reconstruction algorithm that includes these multidimensional MHD terms. This approach is computationally more efficient than previous predictor-corrector based data reconstruction schemes because it does not involve a Riemann problem solution which arises in the usual corrector step [9, 10, 17]. Additionally, it is mathematically more consistent with the governing multidimensional MHD equations than a one-dimension based data reconstruction algorithm used in [10] and [17].

We begin the discussion by the rewriting of the conservative form of equation (11) in primitive variables,

$$Q \frac{\partial \mathbf{V}}{\partial t} + \frac{\partial \mathbf{F}}{\partial \mathbf{U}} Q \frac{\partial \mathbf{V}}{\partial x} + \frac{\partial \mathbf{G}}{\partial \mathbf{U}} Q \frac{\partial \mathbf{V}}{\partial y} = 0, \quad (15)$$

with $\mathbf{U} = Q\mathbf{V}$ such that the matrix Q relates the primitive variables to the conserved ones. Then

$$\frac{\partial \mathbf{V}}{\partial t} + Q^{-1} \frac{\partial \mathbf{F}}{\partial \mathbf{U}} Q \frac{\partial \mathbf{V}}{\partial x} + Q^{-1} \frac{\partial \mathbf{G}}{\partial \mathbf{U}} Q \frac{\partial \mathbf{V}}{\partial y} = 0, \quad (16)$$

gives rise to the exact flux Jacobian matrices,

$$\mathbf{A}_x = Q^{-1} \frac{\partial \mathbf{F}}{\partial \mathbf{U}} Q = Q^{-1} \frac{\partial \mathbf{F}}{\partial \mathbf{V}}, \quad \mathbf{A}_y = Q^{-1} \frac{\partial \mathbf{G}}{\partial \mathbf{U}} Q = Q^{-1} \frac{\partial \mathbf{G}}{\partial \mathbf{V}}, \quad (17)$$

and equation (16) can be written as

$$\frac{\partial \mathbf{V}}{\partial t} + \mathbf{A}_x \frac{\partial \mathbf{V}}{\partial x} + \mathbf{A}_y \frac{\partial \mathbf{V}}{\partial y} = 0. \quad (18)$$

After algebraic manipulations the well-known matrices,

$$\mathbf{A}_x = \begin{pmatrix} u & \rho & 0 & 0 & 0 & 0 & 0 & 0 \\ 0 & u & 0 & 0 & -\frac{B_x}{\rho} & \frac{B_y}{\rho} & \frac{B_z}{\rho} & \frac{1}{\rho} \\ 0 & 0 & u & 0 & -\frac{B_y}{\rho} & -\frac{B_x}{\rho} & 0 & 0 \\ 0 & 0 & 0 & u & -\frac{B_z}{\rho} & 0 & -\frac{B_x}{\rho} & 0 \\ 0 & 0 & 0 & 0 & 0 & 0 & 0 & 0 \\ 0 & B_y & -B_x & 0 & -v & u & 0 & 0 \\ 0 & B_z & 0 & -B_x & -w & 0 & u & 0 \\ 0 & \gamma p & 0 & 0 & -k\mathbf{u} \cdot \mathbf{B} & 0 & 0 & u \end{pmatrix}, \quad (19)$$

$$\mathbf{A}_y = \begin{pmatrix} v & 0 & \rho & 0 & 0 & 0 & 0 & 0 \\ 0 & v & 0 & 0 & -\frac{B_y}{\rho} & -\frac{B_x}{\rho} & 0 & 0 \\ 0 & 0 & v & 0 & \frac{B_x}{\rho} & -\frac{B_y}{\rho} & \frac{B_z}{\rho} & \frac{1}{\rho} \\ 0 & 0 & 0 & v & 0 & -\frac{B_z}{\rho} & -\frac{B_y}{\rho} & 0 \\ 0 & -B_y & B_x & 0 & v & -u & 0 & 0 \\ 0 & 0 & 0 & 0 & 0 & 0 & 0 & 0 \\ 0 & 0 & B_z & -B_y & 0 & -w & v & 0 \\ 0 & 0 & \gamma p & 0 & 0 & -k\mathbf{u} \cdot \mathbf{B} & 0 & v \end{pmatrix}, \quad (20)$$

are obtained, where $k = 1 - \gamma$. Note that, from relations (13) and (14), there are seven non-trivial equations and one trivial equation for which the time derivative becomes zero. This yields the zeros located in each corresponding row in the above 8×8 matrices (19) and (20). In general, the primitive form of the equations can be replaced by a quasi-linear system of equations,

$$\frac{\partial \mathbf{V}}{\partial t} + \bar{\mathbf{A}} \cdot \nabla \mathbf{V} = \frac{\partial \mathbf{V}}{\partial t} + (\bar{\mathbf{A}}_x, \bar{\mathbf{A}}_y) \cdot \nabla \mathbf{V} = 0, \quad (21)$$

where $\bar{\mathbf{A}} \equiv \bar{\mathbf{A}}(\bar{\mathbf{V}}) = \bar{\mathbf{A}}(\mathbf{V}_L, \mathbf{V}_R)$ with left and right states, $\mathbf{V}_L, \mathbf{V}_R$, assuming these and the solution are close to a constant state, $\bar{\mathbf{V}}$.

In one-dimensional MHD the full eight set of MHD equations can be reduced to seven. Should the gradient of the normal magnetic field be zero, such a constant normal field is not to be evaluated. For multidimensional MHD, however, the terms $\partial B_x / \partial x$ and $\partial B_y / \partial y$ do not vanish in general, and play crucial roles that cannot be ignored. Dimensional splitting based on a one-dimensional MHD system of equations lacks these gradient terms and can produce incorrect solutions.

In order to include the gradient terms for multidimensional MHD in a data reconstruction formulation, we present an approach which is built upon a directionally unsplit second-order MUSCL-Hancock algorithm. We treat the evolution of the normal field, B_N , separately from the other primitive variables, i.e., for a case with $B_N = B_x$, define

$$\bar{\mathbf{V}} = \begin{bmatrix} \hat{\mathbf{V}} \\ B_x \end{bmatrix} \text{ and } \bar{\mathbf{A}}_x = \begin{bmatrix} \hat{\mathbf{A}}_x & \mathbf{A}_{B_x} \\ \mathbf{0} & 0 \end{bmatrix}. \quad (22)$$

Here $\hat{\mathbf{V}}$ is a 7×1 vector excluding B_x , $\hat{\mathbf{A}}_x$ is a 7×7 matrix omitting both the fifth row and column in the original matrix \mathbf{A}_x (19), and \mathbf{A}_{B_x} is a 7×1 vector,

$$\mathbf{A}_{B_x} = \left[0, -\frac{B_x}{\rho}, -\frac{B_y}{\rho}, -\frac{B_z}{\rho}, -v, -w, -k\mathbf{u} \cdot \mathbf{B} \right]^T. \quad (23)$$

Similarly, for $B_N = B_y$, $\hat{\mathbf{A}}_y$ is constructed by omitting both the sixth row and column in the original matrix \mathbf{A}_y (20), and \mathbf{A}_{B_y} is

$$\mathbf{A}_{B_y} = \left[0, -\frac{B_x}{\rho}, -\frac{B_y}{\rho}, -\frac{B_z}{\rho}, -u, -w, -k\mathbf{u} \cdot \mathbf{B} \right]^T. \quad (24)$$

A similar approach was adopted by Crockett *et al.* [10] but their equivalent terms for $\hat{\mathbf{A}}_x$ and $\hat{\mathbf{A}}_y$ omitted the factor k in the last entry. The terms \mathbf{A}_{B_x} and \mathbf{A}_{B_y} will be referred to as multidimensional MHD terms in the following. Note that the hat (^) notation has been introduced for the reduced system (i.e., the one corresponding to the usual one-dimensional MHD equation) and the bar (-) notation retained for the re-assembled full system.

The reconstruction of the four multidimensional Riemann states $\mathbf{V}_{i,j,N}^{n+1/2}$, $\mathbf{V}_{i,j,S}^{n+1/2}$, $\mathbf{V}_{i,j,E}^{n+1/2}$ and $\mathbf{V}_{i,j,W}^{n+1/2}$ at cell boundaries, illustrated in Figure 1, is achieved to second-order accuracy by using a TVD MUSCL-Hancock approach. In extrapolating the cell-center values to the cell interfaces we use a TVD slope limiter applied to characteristic variables.

We mention an important strategy for employing TVD limiting at this stage. The limiting is applied to the cell-centered variables, such as density, velocity fields, and pressure, in both normal and transversal directions, while the limiting is applied only in the transversal direction for the cell-centered magnetic fields; hence no limiting is applied to the normal field variables and we directly use the divergence-free field values from the previous time step at the cell-faces. As a consequence, the C^0 continuity of the normal component of the magnetic field at cell-faces is maintained. This strategy is based on numerical considerations to

prevent undesirable jumps in the normal components of the fields at the cell boundaries. Indeed, Powell *et al.* [28] noticed that if the normal fields have jumps at the cell boundaries, the resultant cell-centered field based MHD formulation using a Riemann solver becomes ill-defined. They eventually resolved this by introducing the 8-wave model with modified MHD equations.

In the current scheme using divergence-free cell face-centered fields the continuity consideration of the normal fields at the cell interfaces is thus met straightforwardly.

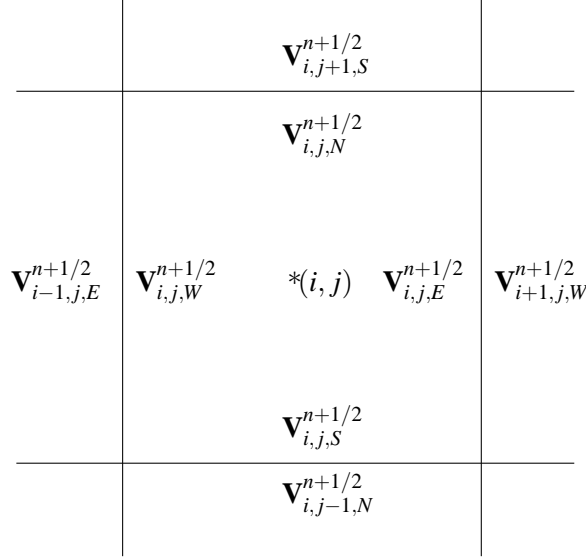


Figure 1: The boundary extrapolated values on a 2D cell geometry. The values are subscripted by N, S, E and W accordingly. These are used as the state values for solving Riemann problem at each cell boundary interface.

Given the quasi-linearized MHD equations,

$$\mathbf{V}_{i,j,E,W}^{n+1/2} = \mathbf{V}_{i,j}^n + \frac{1}{2} [\pm \mathbf{I} - \frac{\Delta t}{\Delta x} \mathbf{A}_x(\mathbf{V}_{i,j}^n)] \Delta_i^n - \frac{\Delta t}{2\Delta y} \mathbf{A}_y(\mathbf{V}_{i,j}^n) \Delta_j^n, \quad (25)$$

$$\mathbf{V}_{i,j,N,S}^{n+1/2} = \mathbf{V}_{i,j}^n - \frac{\Delta t}{2\Delta x} \mathbf{A}_x(\mathbf{V}_{i,j}^n) \Delta_i^n + \frac{1}{2} [\pm \mathbf{I} - \frac{\Delta t}{\Delta y} \mathbf{A}_y(\mathbf{V}_{i,j}^n)] \Delta_j^n, \quad (26)$$

where the plus and minus signs correspond to directions of N, E and S, W respectively, and $\mathbf{A}_x(\mathbf{V}_{i,j}^n)$, $\mathbf{A}_y(\mathbf{V}_{i,j}^n)$ represent matrices calculated at $\mathbf{V}_{i,j}^n$, we first consider data reconstruction in the normal direction (e.g., the first two terms in the left hand side of (25)),

$$\begin{bmatrix} \hat{\mathbf{V}} \\ B_x \end{bmatrix}_{i,j,E,W}^{n+1/2,||} = \begin{bmatrix} \hat{\mathbf{V}} \\ B_x \end{bmatrix}_{i,j}^n + \frac{1}{2} \left(\pm \begin{bmatrix} \hat{\mathbf{I}} & \mathbf{0} \\ \mathbf{0} & 1 \end{bmatrix} - \frac{\Delta t}{\Delta x} \begin{bmatrix} \hat{\mathbf{A}}_x & \mathbf{A}_{B_x} \\ \mathbf{0} & 0 \end{bmatrix}_{i,j} \right) \bar{\Delta}_i^n, \quad (27)$$

where $\bar{\Delta}_i^n = (\hat{\Delta}_i^n, \Delta B_{x,i}^n)^T$ and $\Delta B_{x,i}^n = b_{x,i+1/2,j}^n - b_{x,i-1/2,j}^n$ (the meaning of $\hat{\Delta}_i^n$ becoming clear shortly). The notation B_τ and b_τ denote cell-centered and cell-face magnetic field components respectively, with $\tau = x, y, z$. In the staggered mesh CT algorithm, $\Delta B_{x,i}^n$ is constructed such that the numerical divergence is zero using the cell-centered magnetic fields. In other words, $\Delta B_{x,i}^n$ and $\Delta B_{y,j}^n$ are chosen such that

$$\frac{\Delta B_{x,i}^n}{\Delta x} + \frac{\Delta B_{y,j}^n}{\Delta y} = 0, \quad (28)$$

where we analogously define $\Delta B_{y,j}^n = b_{y,i,j+1/2}^n - b_{y,i,j-1/2}^n$. As noted previously no TVD limiting is applied to $\Delta B_{x,i}^n$ or $\Delta B_{y,j}^n$. Solving (27) is equivalent to considering two subsystems

$$\begin{cases} \hat{\mathbf{V}}_{i,j,E,W}^{n+1/2,\parallel} = \hat{\mathbf{V}}_{i,j}^n + \frac{1}{2} \left(\pm \hat{\mathbf{I}} - \frac{\Delta t}{\Delta x} \hat{\mathbf{A}}_x \right)_{i,j}^n \hat{\Delta}_i^n - \frac{\Delta t}{2\Delta x} (\mathbf{A}_{B_x})_{i,j}^n \Delta B_{x,i}^n, \\ (B_x)_{i,j,E,W}^{n+1/2,\parallel} = B_{x,i,j}^n \pm \frac{1}{2} \Delta B_{x,i}^n. \end{cases} \quad (29)$$

where the second relation in (29) becomes

$$(B_x)_{i,j,E,W}^{n+1/2,\parallel} = B_{x,i,j}^n \pm \frac{1}{2} \Delta B_{x,i}^n = b_{x,i\pm 1/2,j}^n, \quad (30)$$

when the cell-centered magnetic field is reconstructed as

$$B_{x,i,j}^n = \frac{1}{2} \left(b_{x,i+1/2,j}^n + b_{x,i-1/2,j}^n \right). \quad (31)$$

We apply the eigenstructure of the one-dimensional based MHD equations and use characteristic tracing for the first two terms in the first equation in (29). Applying characteristic tracing results in

$$\hat{\mathbf{V}}_{i,j,W}^{n+1/2,\parallel} = \hat{\mathbf{V}}_{i,j}^n + \frac{1}{2} \sum_{k;\lambda_{i,j}^k < 0} \left(-1 - \frac{\Delta t}{\Delta x} \lambda_{i,j}^k \right) \mathbf{r}_{x,i,j}^k \hat{\Delta}_i^n - \frac{\Delta t}{2\Delta x} (\mathbf{A}_{B_x})_{i,j}^n \Delta B_{x,i}^n, \quad (32)$$

$$\hat{\mathbf{V}}_{i,j,E}^{n+1/2,\parallel} = \hat{\mathbf{V}}_{i,j}^n + \frac{1}{2} \sum_{k;\lambda_{i,j}^k > 0} \left(1 - \frac{\Delta t}{\Delta x} \lambda_{i,j}^k \right) \mathbf{r}_{x,i,j}^k \hat{\Delta}_i^n - \frac{\Delta t}{2\Delta x} (\mathbf{A}_{B_x})_{i,j}^n \Delta B_{x,i}^n, \quad (33)$$

with characteristic limiting in the normal direction,

$$\hat{\Delta}_i^n = \text{TVD_Limiter} \left[\mathbf{l}_{x,i,j}^k \cdot \hat{\Delta}_{i,+}^n, \mathbf{l}_{x,i,j}^k \cdot \hat{\Delta}_{i,-}^n \right]. \quad (34)$$

Here $\lambda_{x,i,j}^k, \mathbf{r}_{x,i,j}^k, \mathbf{l}_{x,i,j}^k$ represent the eigenvalue, and the right and left eigenvectors of $\hat{\mathbf{A}}_x$, calculated at the corresponding cell center (i, j) in the x -direction at time step n , and $\hat{\Delta}_{i,+}^n = \hat{\mathbf{V}}_{i+1,j}^n - \hat{\mathbf{V}}_{i,j}^n, \hat{\Delta}_{i,-}^n = \hat{\mathbf{V}}_{i,j}^n - \hat{\mathbf{V}}_{i-1,j}^n$ (similarly for $\hat{\Delta}_{j,\pm}^n$).

The next step includes the transversal flux contribution to the calculated normal state variables. This transversal step, using the eigenstructure of the MHD equations, completes the update from the transversal flux contributions, e.g., the third and second terms in (25) and (26), respectively. For instance, in (25) the transversal step can be updated as

$$\mathbf{V}_{i,j,E,W}^{n+1/2} = \mathbf{V}_{i,j,E,W}^{n+1/2,\parallel} - \frac{\Delta t}{2\Delta y} \mathbf{A}_y (\mathbf{V}_{i,j}^n) \Delta_j^n. \quad (35)$$

Again, this can be written as

$$\begin{bmatrix} \hat{\mathbf{V}} \\ B_y \end{bmatrix}_{i,j,E,W}^{n+1/2} = \begin{bmatrix} \hat{\mathbf{V}} \\ B_y \end{bmatrix}_{i,j,E,W}^{n+1/2,\parallel} - \frac{\Delta t}{2\Delta y} \begin{bmatrix} \hat{\mathbf{A}}_y & \mathbf{A}_{B_y} \\ \mathbf{0} & 0 \end{bmatrix}_{i,j}^n \bar{\Delta}_j^n. \quad (36)$$

This reduces to solving just one subsystem,

$$\hat{\mathbf{V}}_{i,j,E,W}^{n+1/2} = \hat{\mathbf{V}}_{i,j,E,W}^{n+1/2,\parallel} - \frac{\Delta t}{2\Delta y} (\hat{\mathbf{A}}_y)_{i,j}^n \hat{\Delta}_j^n - \frac{\Delta t}{2\Delta y} (\mathbf{A}_{B_y})_{i,j}^n \Delta B_{y,j}^n. \quad (37)$$

Using the eigensystem at the cell center (i, j) in the y -direction, we get,

$$\hat{\mathbf{v}}_{i,j,E,W}^{n+1/2} = \hat{\mathbf{v}}_{i,j,E,W}^{n+1/2,\parallel} - \frac{\Delta t}{2\Delta y} \sum_{k=1}^7 \lambda_{y,i,j}^k \mathbf{r}_{y,i,j}^k \hat{\Delta \alpha}_j^n - \frac{\Delta t}{2\Delta y} (\mathbf{A}_{B_y})_{i,j}^n \Delta B_{y,j}^n, \quad (38)$$

where

$$\hat{\Delta \alpha}_j^n = \text{TVD_Limiter} \left[\mathbf{I}_{y,i,j}^k \cdot \hat{\Delta}_{j,+}^n, \mathbf{I}_{y,i,j}^k \cdot \hat{\Delta}_{j,-}^n \right]. \quad (39)$$

Thus, the four Riemann states $\mathbf{v}_{i,j,N}^{n+1/2}$, $\mathbf{v}_{i,j,S}^{n+1/2}$, $\mathbf{v}_{i,j,E}^{n+1/2}$ and $\mathbf{v}_{i,j,W}^{n+1/2}$ are obtained for each cell. At this stage, however, it should be noticed that upon taking the transversal steps (e.g., in (38)) the C^0 continuity of the normal fields at the cell boundaries imposed in the second equation of the normal steps (e.g., (29) and (30)) have been lost. Maintaining this continuity requirement of the normal fields at the boundaries has been previously recognized as an important issue in the MHD Riemann problem[4, 10, 17]. This requirement is essential for physical consistency when solving the MHD Riemann problem. Computationally, allowing jumps in the normal fields at the cell boundaries can lead to more diffusive solutions to Riemann problems stemming from the upwinding procedure in the Riemann solvers. For the transversal components of the magnetic field, however, discontinuities are allowed and mediate the proper upwinding for them. As a last step, therefore, it is desirable to enforce the continuity of the normal field components at the cell faces, based on the relationship in equation (30). This leads to

$$B_{x,i,j,E}^{n+1/2} = b_{x,i+1/2,j}^n, \quad B_{x,i,j,W}^{n+1/2} = b_{x,i-1/2,j}^n, \quad (40)$$

$$B_{y,i,j,N}^{n+1/2} = b_{y,i,j+1/2}^n, \quad B_{y,i,j,S}^{n+1/2} = b_{y,i,j-1/2}^n. \quad (41)$$

The algorithm for our Riemann state data reconstruction is based on the method of multidimensional characteristic analysis that can be achieved in one single step, without solving any Riemann problem for transversal step. Other recent approaches to obtain second-order accurate approximations of the transversal flux derivatives can be found in [9, 10]. There the transversal updating step used the normal predictor step values to solve another set of two intermediate Riemann problems. The resulting interface fluxes were then used to take numerical derivatives, completing the construction of the second-order Riemann states for evaluating the multidimensional Riemann states.

The current data reconstruction method, which accommodates the MHD eigenstructure multidimensionally in a single step, is simpler and computationally less expensive than the previous approach which uses an extra Riemann solve to evaluate the transversal fluxes. This approach causes no loss of stability for appropriately chosen Courant numbers. The characteristic method is mathematically consistent with the quasi-linearized system of MHD equations.

Another desirable aspect of the current approach can be seen in that the multidimensional terms \mathbf{A}_{B_x} and \mathbf{A}_{B_y} are included such that they are proportional to $\Delta B_{x,i}/\Delta x$ and $\Delta B_{y,j}/\Delta y$. These derivatives are computed using the cell-face magnetic fields that are divergence-free from the CT-type formulation of the USM scheme. This implies that the quantities u, v, w, B_z, p are all evolved proportional to the sum $\frac{\Delta B_{x,i}}{\Delta x} + \frac{\Delta B_{y,j}}{\Delta y}$, which is maintained to be zero numerically (see equation (28)). As a result, this dependence has an important meaning: if perturbations to the divergence $\frac{\Delta B_{x,i}}{\Delta x} + \frac{\Delta B_{y,j}}{\Delta y}$ were to be introduced, such perturbation would affect the behavior of all of u, v, w, B_z, p . For example, as noted by Gardiner *et al.* [17], maintaining planar dynamics in two-dimensional MHD problems and not allowing erroneous growth of the B_z component is directly dependent on how the terms $\Delta B_{x,i}/\Delta x$ and $\Delta B_{y,j}/\Delta y$ are handled in the data reconstruction step. In the current multidimensional predictor-corrector algorithm such growth in B_z is avoided, and its success is illustrated in the in-plane field loop advection test problem of Section 5.

The use of the transversal Godunov flux as in [10] can potentially yield incorrect results. Although [10] used similar multidimensional terms $\mathbf{A}_{B_x} \Delta B_{x,i}^n / \Delta x$ for computing E, W normal states and $\mathbf{A}_{B_y} \Delta B_{y,j}^n / \Delta y$

for N, S normal states, the other set of the multidimensional terms, $\mathbf{A}_{B_y} \Delta B_{y,j}^n / \Delta y$ (for E, W states) and $\mathbf{A}_{B_x} \Delta B_{x,i}^n / \Delta x$ (for N, S states), are not included in the transversal directions; instead the numerical derivative of the transversal fluxes is included. Updating such transversal fluxes can be somewhat similar to including $\mathbf{A}_{B_y} \Delta B_{y,j}^n / \Delta y$ (for E, W states) and $\mathbf{A}_{B_x} \Delta B_{x,i}^n / \Delta x$ (for N, S states), but the transversal fluxes and the multidimensional terms in the normal directions are not canceled identically to ensure the divergence-free property.

Now that the second-order accurate Riemann states, $\mathbf{V}_{i,j,N,S,E,W}^{n+1/2}$, are available second-order Godunov fluxes can be evaluated by solving Riemann problems (RP for short) at cell interfaces. That is,

$$\mathbf{F}_{i-1/2,j}^{*,n+1/2} = \text{RP} \left(\mathbf{V}_{i-1,j,E}^{n+1/2}, \mathbf{V}_{i,j,W}^{n+1/2} \right), \quad \mathbf{F}_{i+1/2,j}^{*,n+1/2} = \text{RP} \left(\mathbf{V}_{i,j,E}^{n+1/2}, \mathbf{V}_{i+1,j,W}^{n+1/2} \right), \quad (42)$$

and

$$\mathbf{G}_{i,j-1/2}^{*,n+1/2} = \text{RP} \left(\mathbf{V}_{i,j-1,N}^{n+1/2}, \mathbf{V}_{i,j,S}^{n+1/2} \right), \quad \mathbf{G}_{i,j+1/2}^{*,n+1/2} = \text{RP} \left(\mathbf{V}_{i,j,N}^{n+1/2}, \mathbf{V}_{i,j+1,S}^{n+1/2} \right). \quad (43)$$

2.2 The USM Cell-centered Solution Update

The algorithm updates the cell-centered conserved variables at time step $n + 1$ using an unsplit single step,

$$\mathbf{U}_{i,j}^{n+1} = \mathbf{U}_{i,j}^n - \frac{\Delta t}{\Delta x} \left\{ \mathbf{F}_{i+1/2,j}^{*,n+1/2} - \mathbf{F}_{i-1/2,j}^{*,n+1/2} \right\} - \frac{\Delta t}{\Delta y} \left\{ \mathbf{G}_{i,j+1/2}^{*,n+1/2} - \mathbf{G}_{i,j-1/2}^{*,n+1/2} \right\}. \quad (44)$$

In general, after this update, non-zero divergence magnetic fields are still present at cell centers. In the following two sections we describe a new modified electric field construction (MEC) scheme and an efficient dissipation control (DC) algorithm for the discrete induction equation that keep the cell-face magnetic fields divergence-free numerically.

The choice of a time step Δt for our unsplit scheme is limited by the CFL condition, (in 2D),

$$\Delta t \left(\frac{|\lambda_{x,i,j}^{\max}|}{\Delta x} + \frac{|\lambda_{y,i,j}^{\max}|}{\Delta y} \right) < c. \quad (45)$$

We use a CFL number of $c = 0.5$ for all calculations, except where otherwise noted.

3 Construction of Electric Fields

A new modified electric field construction (MEC) scheme that demonstrates full directional information is introduced and studied in this section. The MEC scheme is obtained by using the second-order accurate Godunov fluxes that are available in staggered mesh schemes (see [2]). Taylor expansions are applied to the flux components of the magnetic fields (or electric fields by the duality relationship [2]) at the face centers to obtain interpolations at each cell corners, where the electric fields are collocated on a staggered grid. These electric fields are then used in the discrete induction equations to evolve divergenceless magnetic fields at cell-faces.

3.1 Electric Field Averaging Scheme

As already mentioned the CT based scheme requires the evaluation of the electric field \mathbf{E} . Balsara and Spicer [2] proposed to evaluate the electric field on a staggered mesh using high-order Godunov fluxes. There the original arithmetic averaging scheme for the cell-corner (cell edges in three-dimensions) electric field values, uses the duality relationship between the high-order Godunov flux components for magnetic fields and the electric fields. For instance, the negative of the sixth component of the flux in x (equation (13)) and the positive of the fifth component of the flux in y (equation (14)) can be interpreted as the z component

of the electric fields, E_z , at the cell face centers on the staggered grid. Their proposed way to construct E_z at each cell corner was by taking a spatial average directly from this duality relationship through

$$\begin{aligned} E_{z,i+1/2,j+1/2}^{n+1/2} &= \frac{1}{4} \left\{ -F_{6,i+1/2,j}^{*,n+1/2} - F_{6,i+1/2,j+1}^{*,n+1/2} + G_{5,i,j+1/2}^{*,n+1/2} + G_{5,i+1,j+1/2}^{*,n+1/2} \right\} \\ &= \frac{1}{4} \left\{ E_{z,i+1/2,j}^{*,n+1/2} + E_{z,i+1/2,j+1}^{*,n+1/2} + E_{z,i,j+1/2}^{*,n+1/2} + E_{z,i+1,j+1/2}^{*,n+1/2} \right\}, \end{aligned} \quad (46)$$

where the subscripts 6 and 5 denote the sixth and fifth components in the corresponding flux vectors in equations (13)–(14), and the superscript * denotes the fluxes (or flux components) directly from the high-order Godunov schemes. See Figure 2 for the staggered mesh arrangement in two-dimensions.

The electric field E_z in equation (46) can be used to update the induction equation in an appropriate discretization in different MHD solvers. To discretize the induction equation in a more general sense, we consider integrating the differential form (5) over a single three-dimensional control volume $[i - \frac{1}{2}, i + \frac{1}{2}] \times [j - \frac{1}{2}, j + \frac{1}{2}] \times [k - \frac{1}{2}, k + \frac{1}{2}]$ in a Cartesian staggered grid (see Figure 3). Taking a surface integral yields

$$\frac{\partial}{\partial t} \int \int_{\Sigma_\ell \mathcal{F}_\ell} \mathbf{B} \cdot \mathbf{n} dA + \int \int_{\Sigma_\ell \mathcal{F}_\ell} \nabla \times \mathbf{E} \cdot \mathbf{n} dA = 0, \quad (47)$$

where \mathbf{n} is a unit normal vector and the summation is taken over the six bounding faces \mathcal{F}_ℓ , $\ell = 1, \dots, 6$. Then for each face \mathcal{F}_ℓ of the control volume, applying Stokes' Theorem, we get

$$\begin{aligned} \frac{\partial}{\partial t} \int \int_{\mathcal{F}_\ell} \mathbf{B} \cdot \mathbf{n} dA &= - \int \int_{\mathcal{F}_\ell} \nabla \times \mathbf{E} \cdot \mathbf{n} dA \\ &= - \int_{\partial \mathcal{F}_\ell} \mathbf{E} \cdot \mathbf{T} dl \end{aligned} \quad (48)$$

where \mathbf{T} is a unit tangential vector and dl is a line element. Considering the associated normal (denoted by η) and tangential (denoted by τ) components of the magnetic and electric fields for each face \mathcal{F}_ℓ , we let

$$b_\eta^n = \frac{1}{\mu(\mathcal{F}_\ell)} \int \int_{\mathcal{F}_\ell} B_\eta dA, \quad (49)$$

$$E_\tau^{n+1/2} = \frac{1}{\mu(\partial \mathcal{F}_\ell)} \int_{\partial \mathcal{F}_\ell} E_\tau dl, \quad (50)$$

where μ is the Lebesgue measure and $\eta, \tau = x, y, z$. Note that in the CT formulation the magnetic field components b_η^n are the area-averaged values at cell faces, whereas the rest of the conservative variables such as density, momentum, and energy are volume-averaged quantities.

Using (49) and (50) it is straightforward to rewrite the above equation (48) at each control volume's face in component-wise form as

$$\begin{aligned} \Delta y \Delta z \frac{\partial}{\partial t} b_{x,i\pm\frac{1}{2},j,k}^n &= - \left\{ \Delta z (E_{z,i\pm\frac{1}{2},j+\frac{1}{2},k}^{n+1/2} - E_{z,i\pm\frac{1}{2},j-\frac{1}{2},k}^{n+1/2}) + \Delta y (E_{y,i\pm\frac{1}{2},j,k-\frac{1}{2}}^{n+1/2} - E_{y,i\pm\frac{1}{2},j,k+\frac{1}{2}}^{n+1/2}) \right\}, \end{aligned} \quad (51)$$

$$\begin{aligned} \Delta x \Delta z \frac{\partial}{\partial t} b_{y,i,j\pm\frac{1}{2},k}^n &= - \left\{ \Delta z (E_{z,i-\frac{1}{2},j\pm\frac{1}{2},k}^{n+1/2} - E_{z,i+\frac{1}{2},j\pm\frac{1}{2},k}^{n+1/2}) + \Delta x (E_{x,i,j\pm\frac{1}{2},k+\frac{1}{2}}^{n+1/2} - E_{x,i,j\pm\frac{1}{2},k-\frac{1}{2}}^{n+1/2}) \right\}, \end{aligned} \quad (52)$$

$$\begin{aligned} \Delta x \Delta y \frac{\partial}{\partial t} b_{z,i,j,k\pm\frac{1}{2}}^n &= - \left\{ \Delta x (E_{x,i,j-\frac{1}{2},k\pm\frac{1}{2}}^{n+1/2} - E_{x,i,j+\frac{1}{2},k\pm\frac{1}{2}}^{n+1/2}) + \Delta y (E_{y,i+\frac{1}{2},j,k\pm\frac{1}{2}}^{n+1/2} - E_{y,i-\frac{1}{2},j,k\pm\frac{1}{2}}^{n+1/2}) \right\}. \end{aligned} \quad (53)$$

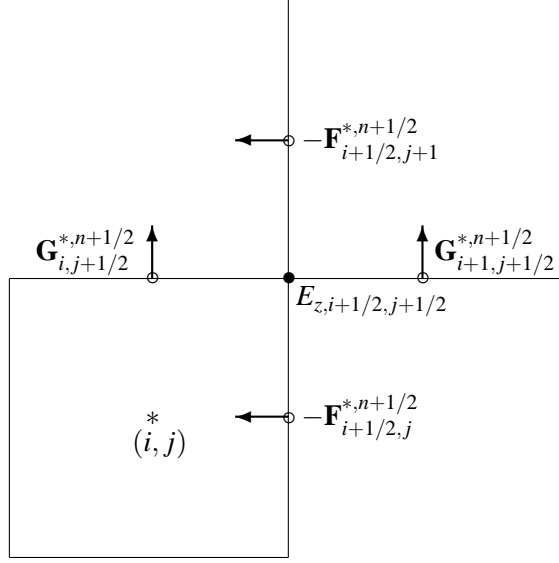


Figure 2: A schematic 2D geometry of the staggered mesh in the flux-CT finite volume scheme. In the staggered mesh, the upwinded numerical fluxes \mathbf{F}^* and \mathbf{G}^* are collocated at the centers of cell interfaces and the electric fields \mathbf{E} (only E_z is shown here for 2D) are collocated at the cell corners.

Further, by discretizing the temporal derivative terms and dividing out Δx , Δy and Δz , we obtain a discrete form of the induction equation on the staggered grid. For instance, in two-dimensions, we get the original Yee method [36] by applying the forward temporal discretization

$$b_{x, i+1/2, j}^{n+1} = b_{x, i+1/2, j}^n - \frac{\Delta t}{\Delta y} \left\{ E_{z, i+1/2, j+1/2}^{n+1/2} - E_{z, i+1/2, j-1/2}^{n+1/2} \right\}, \quad (54)$$

$$b_{y, i, j+1/2}^{n+1} = b_{y, i, j+1/2}^n - \frac{\Delta t}{\Delta x} \left\{ -E_{z, i+1/2, j+1/2}^{n+1/2} + E_{z, i-1/2, j+1/2}^{n+1/2} \right\}. \quad (55)$$

Most CT schemes [2–4, 17] essentially make the above discretization. On a staggered grid, the numerical divergence of \mathbf{B} is defined by

$$(\nabla \cdot \mathbf{B})_{i, j}^{n+1} = \frac{b_{x, i+1/2, j}^{n+1} - b_{x, i-1/2, j}^{n+1}}{\Delta x} + \frac{b_{y, i, j+1/2}^{n+1} - b_{y, i, j-1/2}^{n+1}}{\Delta y} \quad (56)$$

and it remains zero to machine round-off, provided that $(\nabla \cdot \mathbf{B})_{i, j}^n = 0$.

3.2 MEC Algorithm using Directional Derivatives in the Electric Field Construction

A new electric field construction scheme is now described that uses first- and second-order directional derivatives evaluated at cell faces to extrapolate the electric fields to cell corners. The cell-face electric fields are available from corresponding components of the high-order Godunov fluxes that are solutions to the Riemann problem. The superscript “*” is used, consistent with the previous section.

Using a Taylor series expansion of the cell-corner electric field $E_{z, i+1/2, j+1/2}^{n+1/2}$ in all directions, we can

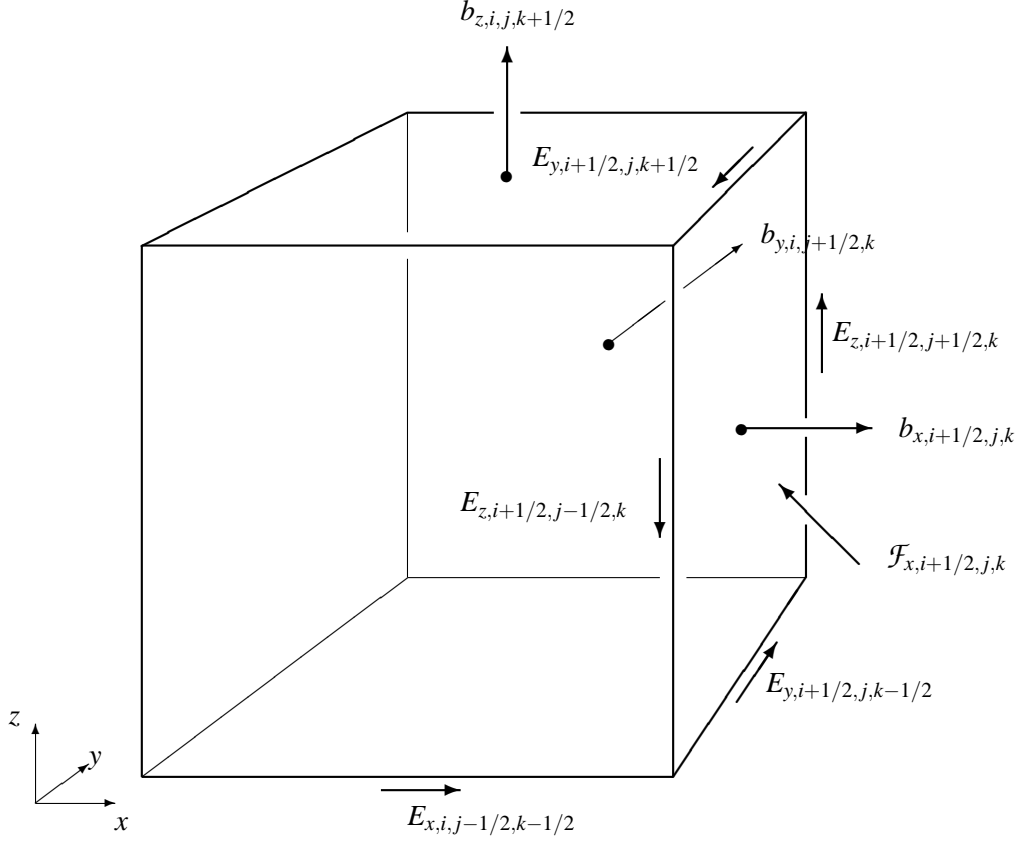


Figure 3: A 3D control volume on the staggered grid with the cell center at (i, j, k) . The magnetic fields are collocated at the cell face centers and the electric fields at the cell edge centers. The line integral of the electric fields $\int_{\partial \mathcal{F}_n} \mathbf{E} \cdot \mathbf{T} dl$ in equation (48) along the four edges of the face $\mathcal{F}_{x,i+1/2,j,k}$ gives rise to the negative of the rate of change of the magnetic field flux in x -direction through the area enclosed by the four edges (e.g., the area of $\mathcal{F}_{x,i+1/2,j,k}$).

write

$$\begin{cases} E_{z,i+1/2,j+1/2}^{n+1/2} = E_{z,i+1/2,j}^{*,n+1/2} + \frac{\Delta y}{2} \frac{\partial E_{z,i+1/2,j}^{*,n+1/2}}{\partial y} + \frac{\Delta y^2}{8} \frac{\partial^2 E_{z,i+1/2,j}^{*,n+1/2}}{\partial y^2} + O(\Delta y^3) \\ E_{z,i+1/2,j+1/2}^{n+1/2} = E_{z,i+1/2,j+1}^{*,n+1/2} - \frac{\Delta y}{2} \frac{\partial E_{z,i+1/2,j+1}^{*,n+1/2}}{\partial y} + \frac{\Delta y^2}{8} \frac{\partial^2 E_{z,i+1/2,j+1}^{*,n+1/2}}{\partial y^2} + O(\Delta y^3), \\ E_{z,i+1/2,j+1/2}^{n+1/2} = E_{z,i,j+1/2}^{*,n+1/2} + \frac{\Delta x}{2} \frac{\partial E_{z,i,j+1/2}^{*,n+1/2}}{\partial x} + \frac{\Delta x^2}{8} \frac{\partial^2 E_{z,i,j+1/2}^{*,n+1/2}}{\partial x^2} + O(\Delta x^3), \\ E_{z,i+1/2,j+1/2}^{n+1/2} = E_{z,i+1,j+1/2}^{*,n+1/2} - \frac{\Delta x}{2} \frac{\partial E_{z,i+1,j+1/2}^{*,n+1/2}}{\partial x} + \frac{\Delta x^2}{8} \frac{\partial^2 E_{z,i+1,j+1/2}^{*,n+1/2}}{\partial x^2} + O(\Delta x^3). \end{cases} \quad (57)$$

The new *modified electric field construction* (MEC) algorithm takes an arithmetic average of these four Taylor expansions, yielding

$$\begin{aligned} & E_{z,i+1/2,j+1/2}^{n+1/2} \\ &= \frac{1}{4} \left\{ E_{z,i+1/2,j}^{*,n+1/2} + \frac{\Delta y}{2} \left(\frac{\partial E_{z,i+1/2,j}^{*,n+1/2}}{\partial y} \right) + \frac{\Delta y^2}{8} \left(\frac{\partial^2 E_{z,i+1/2,j}^{*,n+1/2}}{\partial y^2} \right) \right. \\ & \quad + E_{z,i+1/2,j+1}^{*,n+1/2} - \frac{\Delta y}{2} \left(\frac{\partial E_{z,i+1/2,j+1}^{*,n+1/2}}{\partial y} \right) + \frac{\Delta y^2}{8} \left(\frac{\partial^2 E_{z,i+1/2,j+1}^{*,n+1/2}}{\partial y^2} \right) \\ & \quad \left. + E_{z,i,j+1/2}^{*,n+1/2} + \frac{\Delta x}{2} \left(\frac{\partial E_{z,i,j+1/2}^{*,n+1/2}}{\partial x} \right) + \frac{\Delta x^2}{8} \left(\frac{\partial^2 E_{z,i,j+1/2}^{*,n+1/2}}{\partial x^2} \right) \right\} \end{aligned}$$

$$+E_{z,i+1,j+1/2}^{*,n+1/2} - \frac{\Delta x}{2} \left(\partial E_{z,i+1,j+1/2}^{*,n+1/2} / \partial x \right) + \frac{\Delta x^2}{8} \left(\partial^2 E_{z,i+1,j+1/2}^{*,n+1/2} / \partial x^2 \right) \}. \quad (58)$$

The inclusion of directional derivative terms at this stage has several important aspects. In the CT-type of schemes the magnetic fields (surface variables) are evolved by solving the discretized induction equation (e.g., equations (54) and (55)), whereas other conservative (volumetric) variables such as density, momentum, and energy are updated by solving the underlying high-order Godunov scheme. These two sets of variables are updated differently. This does not mean that the surface and volumetric variables form two decoupled systems; rather, they are strongly coupled via the momentum, energy, and induction equations. Therefore, to obtain an overall accurate solution for both surface and volumetric variables they must be evaluated with consistent high-order accuracy. The derivative terms in equation (58) provide the needed accuracy in comparison to the base construction algorithm (see equation (46)).

The MEC algorithm in (58) is ideally third-order in space for smooth profiles of the electric fields. Note that the base construction scheme only incorporates the smooth part of the electric fields by taking simple arithmetic averages. The situation is improved in the MEC algorithm in such a way that the first derivative terms reflect correct spatial changes from the cell centers to the cell corners. Furthermore, the second derivative terms add consistent amounts of dissipation to the extrapolated cell-corner electric fields, avoiding spurious oscillations near discontinuities in solutions.

To implement the MEC algorithm we discretize the derivative terms. Two different discretization schemes can be considered – central or upwinded differencing. We choose to use a central scheme for two reasons. First, the upwinded differencing requires a wider stencil (one more stencil point for each spatial direction) than central differencing. This means that more guard (or ghost) cells need to be used for an upwinded differencing scheme which is particularly a problem for parallel AMR grid structures where guard cells are used for boundary conditions and updated via inter-processor communications. Further, in multi-dimensions extra guard cells either require more storage or more guard cell copy operations. For high levels of refinement this can be a crucial issue.

Second, an upwinding strategy becomes useful when used to obtain the direction of the propagation of information in a flow field along the characteristics. The electric fields in ideal MHD, $\mathbf{E} = -\mathbf{u} \times \mathbf{B}$, do not propagate along the direction parallel to the velocity field, nor to the magnetic field. Gardiner *et al.* [17] proposed upwinded differencing according to the contact mode at each interface that led to a stable, non-oscillatory integration algorithm. However, having implemented both alternatives we do not find any improvement in the solution using upwinding over central differencing. Thus for physical considerations as well for computational parallel efficiency we choose central differencing for discretizing the derivative terms in the MEC algorithm .

3.3 Central Differencing

Second-order central differencing is considered for both first and second derivative terms in the MEC algorithm. At x interfaces (e.g., at $i \pm \frac{1}{2}$), we can discretize $\partial E_{z,i\pm 1/2,j}^{*,n+1/2} / \partial y$ and $\partial^2 E_{z,i\pm 1/2,j}^{*,n+1/2} / \partial y^2$ as

$$\frac{\partial E_{z,i\pm 1/2,j}^{*,n+1/2}}{\partial y} = \frac{E_{z,i\pm 1/2,j+1}^{*,n+1/2} - E_{z,i\pm 1/2,j-1}^{*,n+1/2}}{2\Delta y}, \quad (59)$$

and

$$\frac{\partial^2 E_{z,i\pm 1/2,j}^{*,n+1/2}}{\partial y^2} = \frac{E_{z,i\pm 1/2,j+1}^{*,n+1/2} - 2E_{z,i\pm 1/2,j}^{*,n+1/2} + E_{z,i\pm 1/2,j-1}^{*,n+1/2}}{\Delta y^2}. \quad (60)$$

Similarly, discretizations at y interfaces (e.g., at $j \pm \frac{1}{2}$) are

$$\frac{\partial E_{z,i,j\pm 1/2}^{*,n+1/2}}{\partial x} = \frac{E_{z,i+1,j\pm 1/2}^{*,n+1/2} - E_{z,i-1,j\pm 1/2}^{*,n+1/2}}{2\Delta x}, \quad (61)$$

and

$$\frac{\partial^2 E_{z,i,j\pm 1/2}^{*,n+1/2}}{\partial x^2} = \frac{E_{z,i+1,j\pm 1/2}^{*,n+1/2} - 2E_{z,i,j\pm 1/2}^{*,n+1/2} + E_{z,i-1,j\pm 1/2}^{*,n+1/2}}{\Delta x^2}. \quad (62)$$

These derivatives are used in (58) the subsequent electric fields are applied to the induction equations (54) and (55) for temporal evolution of the divergence-free magnetic fields. Before proceeding further to solve the induction equation we will introduce in the next section a new dissipation control (DC) algorithm that can be derived from a modification of the induction equation.

3.4 Alternative Averaging Schemes

We conclude this section with several remarks. The *modified flux*-CT scheme of Balsara [4] evaluates the electric field directly at the nodes (e.g., cell corners in 2D, and cell edge centers in 3D) on a staggered grid. That is, in two-dimensions, four Riemann problems are solved to obtain the fluxes at the cell corners and the resulting four flux components are used to construct the cell-corner electric fields directly. This method replaces the spatial averaging scheme in equation (46) with the direct construction scheme. To solve four Riemann problems at these nodal points one first needs to reconstruct four Riemann state variables from the cell-center values. These solves are computationally expensive.

More recently, Gardiner *et al.* [17] introduced a systematic approach to constructing a two-dimensional flux-CT algorithm which is consistent with the underlying plane-parallel, grid-aligned integration algorithm. They addressed the potential inconsistency that can arise from the simple spatial arithmetic averaging scheme of equation (46) for the plane-parallel, grid-aligned flows. Such flows are, for instance, one-dimensional flow problems that are solved on a two-dimensional grid, in which the flow direction is parallel to one of the coordinate axes. Their approach is to add extra terms in the base electric field construction scheme (e.g., equation (46)) in such a way that the electric fields at the cell corners obey the planar symmetry of the plane-parallel, grid-aligned flows. While their scheme is consistent with the underlying flow, it appears to require a greater computational effort than the MEC update scheme does. In their CT algorithm, a two-step procedure is used to update solutions from the n -th to $(n+1)$ -th time step. Thus both the Riemann problem and the electric field construction need to be solved twice each, making their procedure likely more expensive.

4 Efficient Dissipation Control Algorithm for the Induction Equation

A new dissipation control algorithm (DC) is developed by deriving a set of modified equations for the induction equation. The main advantage of the DC is that the method handles numerical anti-dissipations to prevent secular growth in the magnetic field components, especially in the presence of strong gradients in the magnetic field components. A strategy to control numerical dissipation plays a crucial role in many computational simulations. Indeed, for many applications, if the solution does not have enough numerical dissipation implicitly in the algorithm, then the solution becomes unstable unless more dissipation is added explicitly in the calculation. Numerical dissipation is a direct result of the even-order derivatives that exist in the modified equation.

4.1 Modified Equation Analysis of the Induction Equations

It has been shown in the previous section that in the MEC algorithm the second-order derivative terms are added explicitly and introduce the requisite numerical dissipation for the electric fields. It should be realized however, that this dissipation is unrelated to the dissipation that arises in solving the system of the discrete induction equations themselves. To obtain that, we examine the modified equations of the induction equations.

Consider the induction equations in two-dimensions,

$$\frac{1}{\Delta t} \left\{ b_{x,i\pm 1/2,j}^{n+1} - b_{x,i\pm 1/2,j}^n \right\} = \frac{1}{\Delta y} \left\{ -E_{z,i\pm 1/2,j+1/2}^{n+1/2} + E_{z,i\pm 1/2,j-1/2}^{n+1/2} \right\}, \quad (63)$$

$$\frac{1}{\Delta t} \left\{ b_{y,i,j\pm 1/2}^{n+1} - b_{y,i,j\pm 1/2}^n \right\} = \frac{1}{\Delta x} \left\{ E_{z,i+1/2,j\pm 1/2}^{n+1/2} - E_{z,i-1/2,j\pm 1/2}^{n+1/2} \right\}. \quad (64)$$

First, in equation (63), we form Taylor series expansions for $b_{x,i\pm 1/2,j}^{n+1}$, $E_{z,i\pm 1/2,j+1/2}^{n+1/2}$, and $E_{z,i\pm 1/2,j-1/2}^{n+1/2}$ as follows

$$b_{x,i\pm 1/2,j}^{n+1} = b_{x,i\pm 1/2,j}^n + \frac{\partial b_{x,i\pm 1/2,j}^n}{\partial t} \Delta t + \frac{\partial^2 b_{x,i\pm 1/2,j}^n}{\partial t^2} \frac{\Delta t^2}{2} + O(\Delta t^3), \quad (65)$$

$$E_{z,i\pm 1/2,j+1/2}^{n+1/2} = E_{z,i\pm 1/2,j}^{n+1/2} + \frac{\partial E_{z,i\pm 1/2,j}^{n+1/2}}{\partial y} \frac{\Delta y}{2} + \frac{\partial^2 E_{z,i\pm 1/2,j}^{n+1/2}}{\partial y^2} \frac{\Delta y^2}{8} + O(\Delta y^3), \quad (66)$$

$$E_{z,i\pm 1/2,j-1/2}^{n+1/2} = E_{z,i\pm 1/2,j}^{n+1/2} - \frac{\partial E_{z,i\pm 1/2,j}^{n+1/2}}{\partial y} \frac{\Delta y}{2} + \frac{\partial^2 E_{z,i\pm 1/2,j}^{n+1/2}}{\partial y^2} \frac{\Delta y^2}{8} + O(\Delta y^3). \quad (67)$$

Substituting equations (65) – (67) into (63) gives

$$\frac{1}{\Delta t} \left[\frac{\partial b_{x,i\pm 1/2,j}^n}{\partial t} \Delta t + \frac{\partial^2 b_{x,i\pm 1/2,j}^n}{\partial t^2} \frac{\Delta t^2}{2} + O(\Delta t^3) \right] = \frac{1}{\Delta y} \left[-\frac{\partial E_{z,i\pm 1/2,j}^{n+1/2}}{\partial y} \Delta y + O(\Delta y^3) \right]. \quad (68)$$

Rearranging equation (68), we obtain

$$\frac{\partial b_{x,i\pm 1/2,j}^n}{\partial t} + \frac{\partial E_{z,i\pm 1/2,j}^{n+1/2}}{\partial y} = -\frac{\partial^2 b_{x,i\pm 1/2,j}^n}{\partial t^2} \frac{\Delta t}{2} + O(\Delta t^2, \Delta y^2). \quad (69)$$

This equation (69) is the modified equation of the original induction equation (5) and shows that when the difference equation (63) is used it constitutes the solution of a modified PDE, namely equation (69). Comparing with the original PDE of the induction equation (5), equation (69) contains an extra dissipation term (or numerical diffusivity term) $-\partial^2 b_{x,i\pm 1/2,j}^n / \partial t^2$ on the right hand side and this extra term effectively behaves as a source. Since its sign is negative rather than positive, this is an anti-dissipation term and can destabilize the solution or at least cause a loss of accuracy, due to the accumulation of anti-dissipative local truncation error, proportional to Δt , over the simulation time. The effect may be more pronounced near stagnation regions.

To yield useful information, the time derivative on the right hand side of the modified equation (69) can be replaced a by spatial derivative, using the *Cauchy-Kowalewski* procedure. Differentiating equation (69) with respect to t , we can obtain

$$\frac{\partial^2 b_{x,i\pm 1/2,j}^n}{\partial t^2} = -\frac{\partial^2 E_{z,i\pm 1/2,j}^{n+1/2}}{\partial t \partial y} - \frac{\partial^3 b_{x,i\pm 1/2,j}^n}{\partial t^3} \frac{\Delta t}{2} + O(\Delta t^2, \Delta y^2). \quad (70)$$

Substituting (70) from (69) we get

$$\frac{\partial b_{x,i\pm 1/2,j}^n}{\partial t} + \frac{\partial E_{z,i\pm 1/2,j}^{n+1/2}}{\partial y} = \frac{\partial^2 E_{z,i\pm 1/2,j}^{n+1/2}}{\partial t \partial y} \frac{\Delta t}{2} + O(\Delta t^2, \Delta y^2). \quad (71)$$

In general, for linear advection, $\frac{\partial u}{\partial t} + a \frac{\partial u}{\partial x} = 0$, all the time derivatives in a modified equation can be replaced with the spatial derivatives by repeatedly differentiating the linear modified equation, to obtain

corresponding spatial derivatives instead. By contrast, the induction equation is nonlinear and the time derivative in $\partial^2 E_{z,i\pm 1/2,j}^{n+1/2} / \partial t \partial y$ can not be completely replaced by the spatial derivative. To overcome this difficulty and accomplish an efficient dissipation control algorithm, we retain the time derivative and use that derivative information.

For completeness we present the modified equation of the induction equation for the y component magnetic field,

$$\frac{\partial b_{y,i,j\pm 1/2}^n}{\partial t} + \frac{\partial \left(-E_{z,i,j\pm 1/2}^{n+1/2} \right)}{\partial x} = \frac{\partial^2 \left(-E_{z,i,j\pm 1/2}^{n+1/2} \right)}{\partial t \partial x} \frac{\Delta t}{2} + O(\Delta t^2, \Delta x^2). \quad (72)$$

4.2 Difference Equations for the Dissipation-Control Algorithm

The derivation of the modified equations allow a consistent discretization scheme that uses the dissipation terms in the DC scheme. We choose an explicit forward time centered space (FTCS) discretization for the terms $\frac{\partial^2}{\partial t \partial y} E_{z,i\pm 1/2,j}^{n+1/2}$ and $\frac{\partial^2}{\partial t \partial x} \left(-E_{z,i,j\pm 1/2}^{n+1/2} \right)$ in equations (71) and (72). For the rest of the derivative terms on the left hand side of equations (71) and (72), we retain the original scheme (which in fact is also FTCS) as discretized in equations (63) and (64), because the derived modified equations stem from that discretization.

Equations (71) and (72) are discretized in an FTCS manner below. To control the anti-dissipative effect of the term $\frac{\partial^2}{\partial t \partial y} E_{z,i\pm 1/2,j}^{n+1/2}$ in the x component equation (71), a corresponding *dissipative* contribution is made by adding an equivalent term with an opposite sign. In practice, $\frac{\partial^2}{\partial t \partial y} E_{z,i\pm 1/2,j}^{n+1/2} \frac{\Delta t}{2}$ in equation (71) is replaced with $-\frac{\partial^2}{\partial t \partial y} E_{z,i\pm 1/2,j}^{n+1/2} \frac{\Delta t}{2}$. First, we discretize the derivative as follows,

$$\begin{aligned} -\frac{\partial^2 E_{z,i\pm 1/2,j}^{n+1/2}}{\partial t \partial y} &= -\frac{\partial}{\partial t} \frac{1}{\Delta y} \left\{ E_{z,i\pm 1/2,j+1/2}^{n+1/2} - E_{z,i\pm 1/2,j-1/2}^{n+1/2} \right\} \\ &= -\frac{1}{\Delta t \Delta y} \left\{ \left(E_{z,i\pm 1/2,j+1/2}^{n+1/2} - E_{z,i\pm 1/2,j-1/2}^{n+1/2} \right) \right. \\ &\quad \left. - \left(E_{z,i\pm 1/2,j+1/2}^{n-1/2} - E_{z,i\pm 1/2,j-1/2}^{n-1/2} \right) \right\}. \end{aligned} \quad (73)$$

Note that the cell-corner electric fields $E_{z,i\pm 1/2,j\pm 1/2}^{n+1/2}$ are available from the MEC scheme (58). Multiplying by $\Delta t/2$ the above equation (73), according to (71), we get

$$\begin{aligned} \frac{1}{\Delta t} \left\{ b_{x,i\pm 1/2,j}^{n+1} - b_{x,i\pm 1/2,j}^n \right\} &= -\frac{1}{\Delta y} \left\{ E_{z,i\pm 1/2,j+1/2}^{n+1/2} - E_{z,i\pm 1/2,j-1/2}^{n+1/2} \right\} \\ &\quad - \frac{1}{2\Delta y} \left\{ \left(E_{z,i\pm 1/2,j+1/2}^{n+1/2} - E_{z,i\pm 1/2,j-1/2}^{n+1/2} \right) \right. \\ &\quad \left. - \left(E_{z,i\pm 1/2,j+1/2}^{n-1/2} - E_{z,i\pm 1/2,j-1/2}^{n-1/2} \right) \right\}. \end{aligned} \quad (74)$$

Rearranging equation (74), the final form of the x component induction equation for the DC scheme yields

$$\begin{aligned} b_{x,i\pm 1/2,j}^{n+1} &= b_{x,i\pm 1/2,j}^n - \frac{\Delta t}{\Delta y} \left\{ E_{z,i\pm 1/2,j+1/2}^{n+1/2} - E_{z,i\pm 1/2,j-1/2}^{n+1/2} \right\} \\ &\quad - \frac{\Delta t}{2\Delta y} \left\{ \left(E_{z,i\pm 1/2,j+1/2}^{n+1/2} - E_{z,i\pm 1/2,j-1/2}^{n+1/2} \right) \right. \\ &\quad \left. - \left(E_{z,i\pm 1/2,j+1/2}^{n-1/2} - E_{z,i\pm 1/2,j-1/2}^{n-1/2} \right) \right\}. \end{aligned} \quad (75)$$

Similarly, the y component equation (72), leads to,

$$\begin{aligned}
b_{y,i,j\pm 1/2}^{n+1} &= b_{y,i,j\pm 1/2}^n - \frac{\Delta t}{\Delta x} \left\{ -E_{z,i+1/2,j\pm 1/2}^{n+1/2} + E_{z,i-1/2,j\pm 1/2}^{n+1/2} \right\} \\
&\quad - \frac{\Delta t}{2\Delta x} \left\{ \left(-E_{z,i+1/2,j\pm 1/2}^{n+1/2} + E_{z,i-1/2,j\pm 1/2}^{n+1/2} \right) \right. \\
&\quad \left. - \left(-E_{z,i+1/2,j\pm 1/2}^{n-1/2} + E_{z,i-1/2,j\pm 1/2}^{n-1/2} \right) \right\}. \tag{76}
\end{aligned}$$

The advantages of using the FTCS method (as opposed to, for instance, using the backward time centered space or BTCS) for $\frac{\partial^2}{\partial t \partial y} E_{z,i\pm 1/2,j}^{n+1/2}$ and $\frac{\partial^2}{\partial t \partial x} \left(-E_{z,i,j\pm 1/2}^{n+1/2} \right)$ are threefold: First, the choice is consistent with the discretization originally used for the derivatives in (63) and (64); second, the centered in space discretization is also consistent with physical considerations, in that the electric field is evaluated via Stokes' Theorem, followed by line integrals, resulting in the same formulation as equations (51) and (52); finally, the FTCS scheme as applied to $\frac{\partial^2}{\partial t \partial y} E_{z,i\pm 1/2,j}^{n+1/2}$ and $\frac{\partial^2}{\partial t \partial x} \left(-E_{z,i,j\pm 1/2}^{n+1/2} \right)$ requires the smallest possible stencil size in both space and time. The centered in space discretization only utilizes two cell-corner electric field values that are always available within each cell. Thus, there is no need to obtain the cell-neighbor information and the scheme is local. Not only does this effect computational efficiency, but also guarantees preservation of the divergence-free constraint of the DC scheme. For example, if another spatial discretization requiring a wider stencil such as an upwinding method were chosen, the spatial discretization would also require each cell's neighbor information, which ultimately breaks the symmetry relationship that should be preserved to maintain the divergence-free constraint. In the next subsection, we show that the DC scheme developed in equations (75) and (76) indeed satisfies the divergence-free property.

Summarizing, the second-order in time and space dissipation controls for the induction equations are made available by modified equation analysis. The anti-dissipative relationship has been elucidated, which has been heretofore neglected in previous MHD schemes. Such anti-dissipation controls recover the proper dissipation relationship by balancing the anti-dissipation terms with oppositely signed dissipative terms in the modified induction equation. To incorporate the dissipation, the DC scheme uses FTCS differencing, which has distinct advantages, to discretize the related temporal and spatial derivatives. The DC scheme, thus explicitly controls the anti-dissipative phenomena in the evolution of the cell-face magnetic fields. Lastly, the DC scheme can be incorporated in other CT based schemes without significant overhead. In Section 5, we show that there are crucial improvements in the magnetic field solutions due to incorporating the DC scheme.

We can further parameterize the dissipation terms in equations (75) and (76). Choosing a dissipation parameter, $0 \leq \nu \leq 1$, the parameterized dissipation relations for the DC scheme become

$$\begin{aligned}
b_{x,i\pm 1/2,j}^{n+1} &= b_{x,i\pm 1/2,j}^n - \frac{\Delta t}{\Delta y} \left\{ E_{z,i\pm 1/2,j+1/2}^{n+1/2} - E_{z,i\pm 1/2,j-1/2}^{n+1/2} \right\} \\
&\quad - \nu \frac{\Delta t}{2\Delta y} \left\{ \left(E_{z,i\pm 1/2,j+1/2}^{n+1/2} - E_{z,i\pm 1/2,j-1/2}^{n+1/2} \right) \right. \\
&\quad \left. - \left(E_{z,i\pm 1/2,j+1/2}^{n-1/2} - E_{z,i\pm 1/2,j-1/2}^{n-1/2} \right) \right\}, \tag{77}
\end{aligned}$$

$$\begin{aligned}
b_{y,i,j\pm 1/2}^{n+1} &= b_{y,i,j\pm 1/2}^n - \frac{\Delta t}{\Delta x} \left\{ -E_{z,i+1/2,j\pm 1/2}^{n+1/2} + E_{z,i-1/2,j\pm 1/2}^{n+1/2} \right\} \\
&\quad - \nu \frac{\Delta t}{2\Delta x} \left\{ \left(-E_{z,i+1/2,j\pm 1/2}^{n+1/2} + E_{z,i-1/2,j\pm 1/2}^{n+1/2} \right) \right. \\
&\quad \left. - \left(-E_{z,i+1/2,j\pm 1/2}^{n-1/2} + E_{z,i-1/2,j\pm 1/2}^{n-1/2} \right) \right\}. \tag{78}
\end{aligned}$$

In this parametrized form it is clear that when $\nu = 0$ the DC scheme results in standard discrete induction

equations. Unless otherwise stated, we refer to equations (77) and (78) as the *the DC equations* in the rest of this paper.

4.3 Initial Condition of the DC Equations

Since the DC equations make use of the electric fields from the previous time step, the electric fields needs to be initialized before the first update. This is contrast to the base CT scheme where initialization is not needed. A simple choice for an initial condition of the electric fields can be obtained by using the relationship $\mathbf{E} = -\mathbf{u} \times \mathbf{B}$ directly. After initializing the cell-centered velocity and magnetic fields, we obtain

$$u_{i+1/2,j+1/2}^0 = \frac{1}{4} (u_{i,j}^0 + u_{i+1,j}^0 + u_{i,j+1}^0 + u_{i+1,j+1}^0), \quad (79)$$

$$v_{i+1/2,j+1/2}^0 = \frac{1}{4} (v_{i,j}^0 + v_{i+1,j}^0 + v_{i,j+1}^0 + v_{i+1,j+1}^0), \quad (80)$$

$$B_{x,i+1/2,j+1/2}^0 = \frac{1}{2} (b_{x,i+1/2,j}^0 + b_{x,i+1/2,j+1}^0), \quad (81)$$

$$B_{y,i+1/2,j+1/2}^0 = \frac{1}{2} (b_{y,i,j+1/2}^0 + b_{y,i+1,j+1/2}^0). \quad (82)$$

Then the cell-corner electric fields are initialized* as

$$E_{z,i+1/2,j+1/2}^0 = v_{i+1/2,j+1/2}^0 B_{x,i+1/2,j+1/2}^0 - u_{i+1/2,j+1/2}^0 B_{y,i+1/2,j+1/2}^0. \quad (83)$$

A choice for a non-zero value of \mathbf{v} is made in Section 5 in our test suite simulations.

4.4 Demonstration of the Divergence-Free Property of FTCS for DC

In this section, a demonstration of the divergence-free property for the DC equations is presented. We assume that $(\nabla \cdot \mathbf{B})_{(i,j)}^n = 0$ initially at time step n . Then

$$\begin{aligned} (\nabla \cdot \mathbf{B})_{i,j}^{n+1} &= \frac{b_{x,i+1/2,j}^{n+1} - b_{x,i-1/2,j}^{n+1}}{\Delta x} + \frac{b_{y,i,j+1/2}^{n+1} - b_{y,i,j-1/2}^{n+1}}{\Delta y} \\ &= \frac{1}{\Delta x} \left\{ b_{x,i+1/2,j}^n - \frac{\Delta t}{\Delta y} (E_{z,i+1/2,j+1/2}^{n+1/2} - E_{z,i+1/2,j-1/2}^{n+1/2}) \right. \\ &\quad \left. - v \frac{\Delta t}{2\Delta y} [E_{z,i+1/2,j+1/2}^{n+1/2} - E_{z,i+1/2,j-1/2}^{n+1/2} - E_{z,i+1/2,j+1/2}^{n-1/2} + E_{z,i+1/2,j-1/2}^{n-1/2}] \right. \\ &\quad \left. - b_{x,i-1/2,j}^n + \frac{\Delta t}{\Delta y} (E_{z,i-1/2,j+1/2}^{n+1/2} - E_{z,i-1/2,j-1/2}^{n+1/2}) \right. \\ &\quad \left. + v \frac{\Delta t}{2\Delta y} [E_{z,i-1/2,j+1/2}^{n+1/2} - E_{z,i-1/2,j-1/2}^{n+1/2} - E_{z,i-1/2,j+1/2}^{n-1/2} + E_{z,i-1/2,j-1/2}^{n-1/2}] \right\} \\ &+ \frac{1}{\Delta y} \left\{ b_{y,i,j+1/2}^n - \frac{\Delta t}{\Delta x} (-E_{z,i+1/2,j+1/2}^{n+1/2} + E_{z,i-1/2,j+1/2}^{n+1/2}) \right. \\ &\quad \left. + v \frac{\Delta t}{2\Delta x} [-E_{z,i+1/2,j+1/2}^{n+1/2} + E_{z,i-1/2,j+1/2}^{n+1/2} + E_{z,i+1/2,j+1/2}^{n-1/2} - E_{z,i-1/2,j+1/2}^{n-1/2}] \right. \\ &\quad \left. - b_{y,i,j-1/2}^n + \frac{\Delta t}{\Delta x} (-E_{z,i+1/2,j-1/2}^{n+1/2} + E_{z,i-1/2,j-1/2}^{n+1/2}) \right. \\ &\quad \left. - v \frac{\Delta t}{2\Delta x} [-E_{z,i+1/2,j-1/2}^{n+1/2} + E_{z,i-1/2,j-1/2}^{n+1/2} + E_{z,i+1/2,j-1/2}^{n-1/2} - E_{z,i-1/2,j-1/2}^{n-1/2}] \right\} \end{aligned}$$

*In a departure from our previous notation, we let $E_{z,i+1/2,j+1/2}^0 \equiv E_{z,i+1/2,j+1/2}^{-1/2}$ in (77) and (78) for $n = 0$.

$$\begin{aligned}
&= \frac{b_{x,i+1/2,j}^n - b_{x,i-1/2,j}^n}{\Delta x} + \frac{b_{y,i,j+1/2}^n - b_{y,i,j-1/2}^n}{\Delta y} \\
&+ \frac{\Delta t}{\Delta x \Delta y} \left\{ -E_{z,i+1/2,j+1/2}^{n+1/2} + E_{z,i+1/2,j-1/2}^{n+1/2} + E_{z,i-1/2,j+1/2}^{n+1/2} - E_{z,i-1/2,j-1/2}^{n+1/2} \right. \\
&\quad \left. + E_{z,i+1/2,j+1/2}^{n+1/2} - E_{z,i-1/2,j+1/2}^{n+1/2} - E_{z,i+1/2,j-1/2}^{n+1/2} + E_{z,i-1/2,j-1/2}^{n+1/2} \right\} \\
&+ v \frac{\Delta t}{2\Delta x \Delta y} \left\{ -E_{z,i+1/2,j+1/2}^{n+1/2} + E_{z,i+1/2,j-1/2}^{n+1/2} + E_{z,i-1/2,j+1/2}^{n+1/2} - E_{z,i-1/2,j-1/2}^{n+1/2} \right. \\
&\quad \left. + E_{z,i+1/2,j+1/2}^{n-1/2} - E_{z,i+1/2,j-1/2}^{n-1/2} - E_{z,i-1/2,j+1/2}^{n-1/2} + E_{z,i-1/2,j-1/2}^{n-1/2} \right. \\
&\quad \left. + E_{z,i+1/2,j+1/2}^{n+1/2} - E_{z,i-1/2,j+1/2}^{n+1/2} - E_{z,i+1/2,j-1/2}^{n+1/2} + E_{z,i-1/2,j-1/2}^{n+1/2} \right. \\
&\quad \left. - E_{z,i+1/2,j+1/2}^{n-1/2} + E_{z,i-1/2,j+1/2}^{n-1/2} + E_{z,i+1/2,j-1/2}^{n-1/2} - E_{z,i-1/2,j-1/2}^{n-1/2} \right\} \\
&= (\nabla \cdot \mathbf{B})_{i,j}^n \\
&= 0.
\end{aligned}$$

Note that the symmetry relationship gives a perfect cancellation of the electric fields which leads to the divergence-free property in the discrete form. As noted earlier the DC scheme's divergence-free property is preserved locally, so that the constraint is straightforwardly maintained on AMR block structures.

4.5 Reconstruction of Cell-Centered Fields

By solving the DC equations, the dissipation controlled, divergence-free cell-face magnetic fields are made available. To update other volumetric variables in the CT-type of Godunov based MHD solver, we reconstruct the cell-centered magnetic fields as follows. In the base CT scheme of Balsara and Spicer [2], and other CT schemes, the volume-averaged magnetic field components at cell centers are obtained by taking the arithmetic average of the cell-face, divergence-free magnetic fields as

$$B_{x,i,j}^n = \frac{1}{2} \left(b_{x,i-1/2,j}^n + b_{x,i+1/2,j}^n \right), \quad (84)$$

$$B_{y,i,j}^n = \frac{1}{2} \left(b_{y,i,j-1/2}^n + b_{y,i,j+1/2}^n \right). \quad (85)$$

In this reconstruction step, the divergence-free constraint for the cell-centered fields is no longer preserved. Therefore, although the divergenceless evolution of the face centered fields are ensured after each DC step, numerical monopoles are still introduced in the cell-centered fields. To overcome this, Balsara [3,4] has proposed a reconstruction algorithm that ensures the divergence-free property for the cell-centered magnetic fields which uses

$$B_{x,i,j}^n = \frac{1}{2} \left(b_{x,i-1/2,j}^n + b_{x,i+1/2,j}^n \right) - a_{xx} \frac{\Delta x^2}{6}, \quad (86)$$

$$B_{y,i,j}^n = \frac{1}{2} \left(b_{y,i,j-1/2}^n + b_{y,i,j+1/2}^n \right) - c_{yy} \frac{\Delta y^2}{6}, \quad (87)$$

where the nonzero coefficients a_{xx} and c_{yy} are described therein. Although the approach has advantage in guaranteeing the divergence-free constraint for the cell-centered fields, it is clear from (86) and (87) that the base reconstruction scheme in (84) and (85) are sufficient for a second-order scheme[†]. Thus our USM-MEC-DC scheme uses (84) and (85) by default.

[†]In fact, it has been reported in [22] that there is no noticeable difference between the results of using the base scheme (84) and (85) and the newer (86) and (87).

Summarizing the advantages of using the MEC-DC approach, we note: First, the method provides discrete divergence-free fields in real space up to machine round-off error over the entire computational domain; second, because the divergence-free constraint is met in real space, the resultant magnetic fields are physically meaningful in a continuous sense over the domain. This is in contrast to the vector divergence-cleaning method, in which the divergence-free property of the fields can be viewed only at discrete points in Fourier space; third, the local property of the divergence-free fields enables minimal inter-communication on parallel machines, and thus an extension to block-refined parallel AMR is straightforward; fourth, issues of solving an elliptic Poisson equation, and associated possible aliasing issues if FFTs are used for the purpose, are eliminated; lastly, a new way to control anti-dissipation, which can potentially be used in other schemes when solving the induction equation, has been explored. By including corresponding dissipation terms, unphysical growth of the magnetic fields is obviated in an efficient manner. The importance of keeping the dissipation control terms is shown to be crucial in some MHD simulations in the test suite described in Section 5.

5 Numerical Results

Validation studies of the USM-MEC-DC scheme have been made with a suite of MHD test problems. A series of numerical studies show that the scheme is second-order accurate, and maintains the solenoidal constraint of magnetic fields up to machine round-off error. The CFL number of 0.5 is used in all simulations except that a lower value 0.3 is found to lead to stability in the cloud-shock interaction problem for capturing the strong interaction. In all of the multidimensional problems presented using the new scheme, both MEC and DC have been used, and the multidimensional characteristic method in the data reconstruction-evolution step utilized. Their roles are pointed out and found to be of importance.

5.1 Field Loop Problem

The first test is the field loop problem [17] which is a severe test case in multidimensional MHD. This test problem considers two different initial conditions of a weakly polarized magnetic field loop: the loop is either advected with the flow or held stationary. The first case of this test problem, with advection, is more stringent than the second case with just diffusion, since it is more difficult to preserve the circular shape of the advecting field loop as it traverses the computational domain during the simulation. In the second case, that of the diffusion test, the only dynamics present is numerical diffusion and determines how diffusivity of the scheme. In both cases, an insufficient amount of numerical dissipation can distort the circular shape of the field loop.

We follow the parameters of Gardiner & Stone [17,33]. The computational domain is $[-1, 1] \times [-0.5, 0.5]$, with a mesh 256×148 , and doubly-periodic boundary conditions. The density and pressure are set to unity everywhere and $\gamma = 5/3$. The velocity fields are defined as,

$$\mathbf{U} = u_0(\cos\theta, \sin\theta, 0) \quad (88)$$

with the advection angle θ , given by $\theta = \tan^{-1}(0.5) \approx 26.57^\circ$. The choices for the initial velocity were set as $u_0 = \sqrt{5}$ for the advection test and $u_0 = 0$ for the diffusion test. The size of domain and other parameters were chosen such that, for the advection case, the weakly magnetized field loop makes one complete cycle by $t = 1$. To initialize $\nabla \cdot \mathbf{B} = 0$ numerically, the components of the magnetic field values are obtained by taking the numerical curl of the z -component of the magnetic vector potential A_z

$$\frac{\partial A_z}{\partial x} = -B_y, \quad \frac{\partial A_z}{\partial y} = B_x, \quad (89)$$

where

$$A_z = \begin{cases} A_0(R-r) & \text{if } r \leq R, \\ 0 & \text{otherwise} \end{cases}. \quad (90)$$

By using this initialization process, divergence-free magnetic fields are constructed with a maximum value of $\nabla \cdot \mathbf{B}$ on the order of 10^{-16} at the chosen resolution. The parameters in (90) are $A_0 = 10^{-3}$, $R = 0.3$ with a field loop radius R . This initial condition results in a very high beta plasma $\beta = 2p/B^2 = 2 \times 10^6$ for the inner region of the field loop. Inside the loop the magnetic field strength is very weak and the flow dynamics is dominated by the gas pressure.

The first test of the advection case is integrated to a final time $t = 2$. The advection test is found to truly require the full multidimensional MHD approach, i.e., the inclusion of the multidimensional terms (23) and (24) as described in Section 2. Since the field loop is advected at an oblique angle to the x -axis of the computational domain, the values of $\partial B_x/\partial x$ and $\partial B_y/\partial y$ are non-zero in general, and these terms together with the multidimensional terms $\mathbf{A}_{B_x}, \mathbf{A}_{B_y}$ are included.

The flow advects the field loop with the given advection angle to the grid. During the advection a good numerical scheme should maintain the circular symmetry of the loop at all time. A lack of proper numerical dissipation results in spurious oscillations at the loop, breaking the circular symmetry. Shown in Figure 4 are the initial conditions of the current density, the magnetic field lines (20 contour lines of A_z are shown), and the magnetic pressure. The DC scheme (77) and (78) with a default value of $\nu = 0.5$ was used.

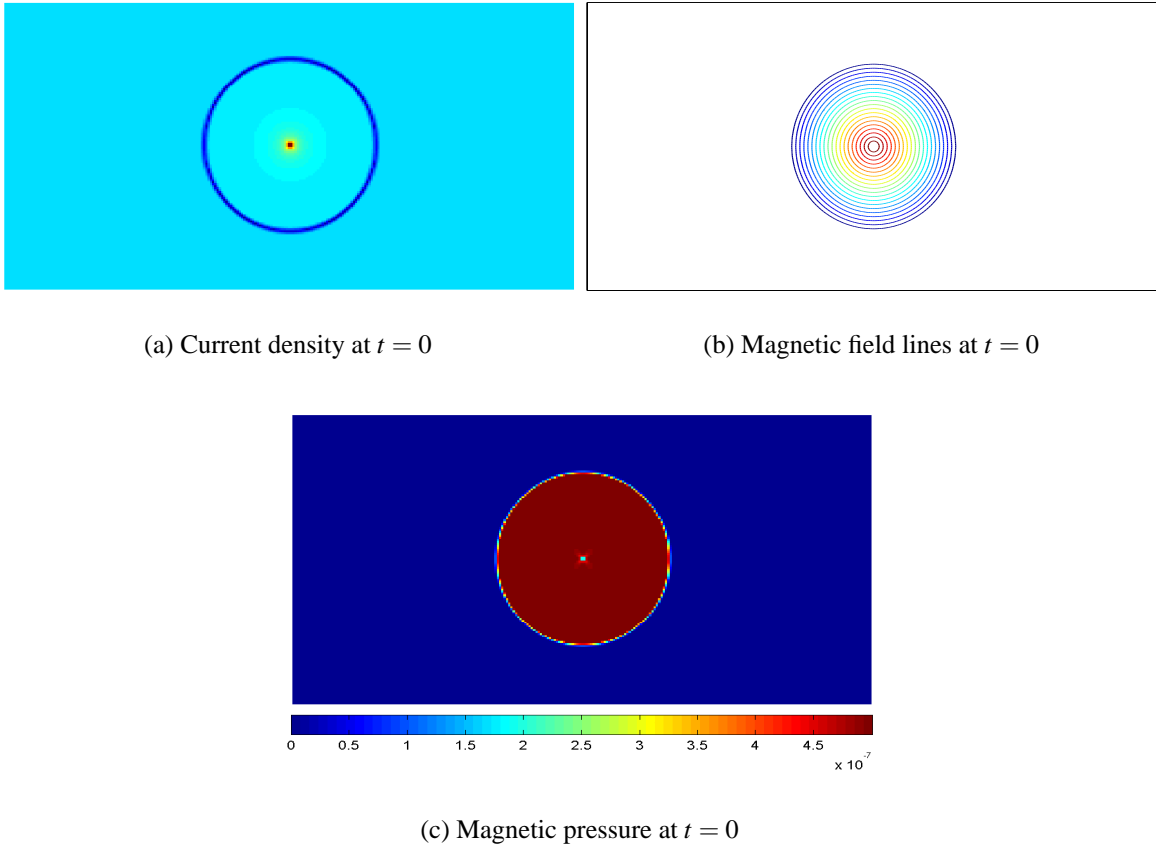


Figure 4: The initial conditions of the field loop advection problem with 256×148 resolution.

From the results in Figure 5, the USM-MEC-DC scheme maintains the circular shape of the loop extremely well to the final time step. The first plot is of the current density \mathbf{j} which, being the curl of the field components, is very sensitive to oscillations in these components. The USM-MEC-DC scheme successfully retains the initial circular symmetry and does not develop severe oscillations. In the second plot (b) 20 field lines are still evident in the final solution, maintaining the original circular symmetry. There is only slight dissipation apparent at the very center, leading to the disappearance of the smallest circular field line contour. The final magnetic pressure $B_p = (B_x^2 + B_y^2)/2$, shown in (c), compares well with the results of Gardiner *et al.* [17]. The results obtained here lead us to conclude that the anti-dissipation control of the DC scheme plays an essential role in achieving the appropriate amount of numerical dissipation of the magnetic field components.

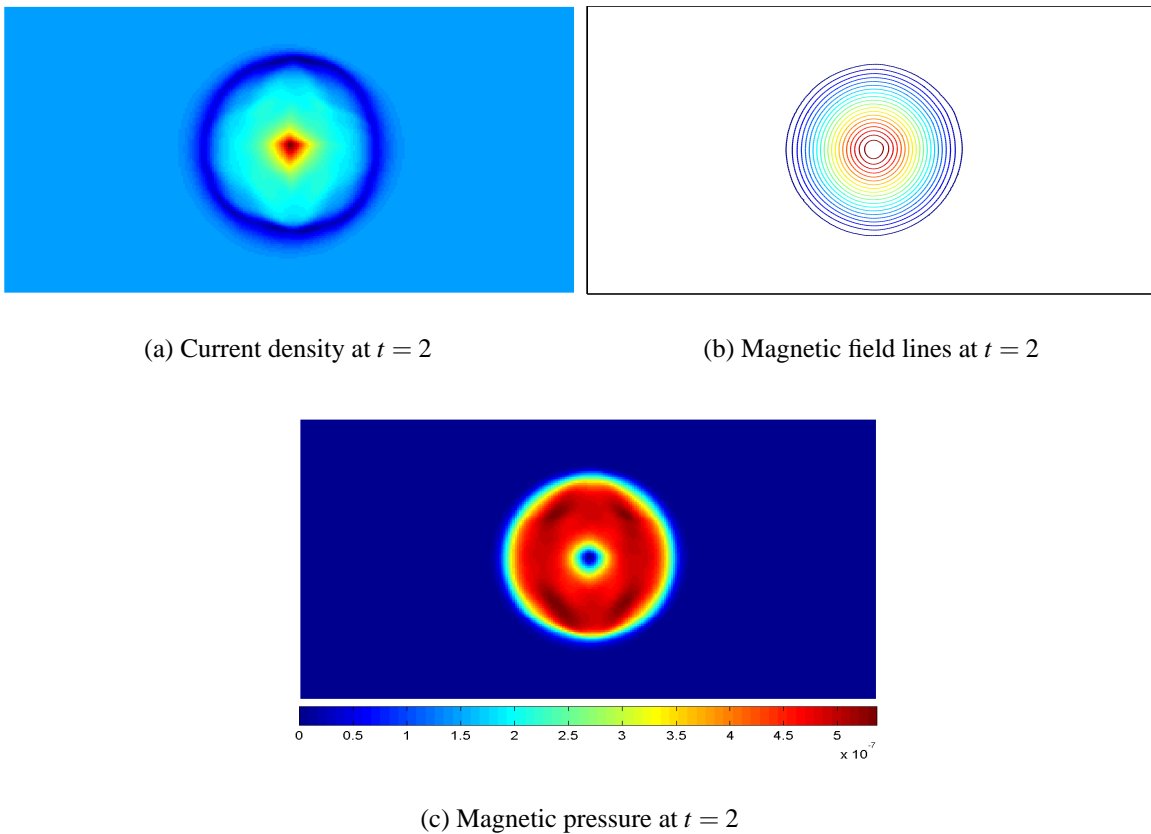
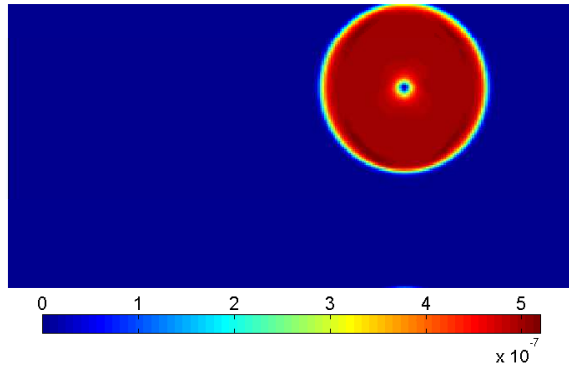


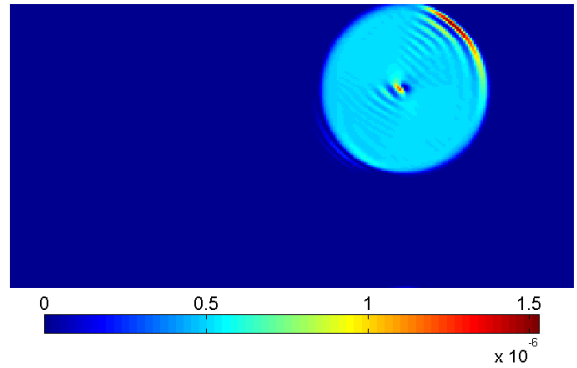
Figure 5: The field loop advection problem at time $t = 2$. The value $\nu = 0.5$ is used.

To amplify on the role of the DC treatment, the results obtained without turning on the DC switch ($\nu = 0$) is presented in Figure 6. In plot (b) the magnetic pressure already suffers from strong oscillations over the entire loop even at a relatively earlier time, $t = 0.2$. Note also that the magnitude of the magnetic pressure is increased by an order of magnitude as a consequence of the absence of anti-dissipation control in the scheme. The final solution in (c) is quite disastrous, leaving no trace of the initial circular shape. The magnitude reaches up to 0.12 which is an order of 10^7 larger than the initial value (See the initial magnitude in (c) in Figure 4.)

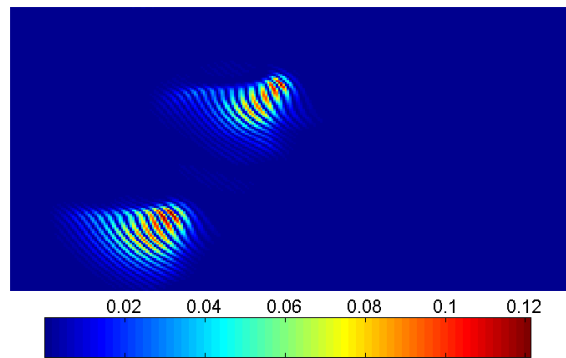
We also examine the effect of the value of ν in the DC scheme, and consider the same advection problem using the maximum value of $\nu = 1$. This larger value clearly gives more dissipation that prevents further



(a) Magnetic pressure at $t = 0.2$ with DC



(b) Magnetic pressure at $t = 0.2$ without DC

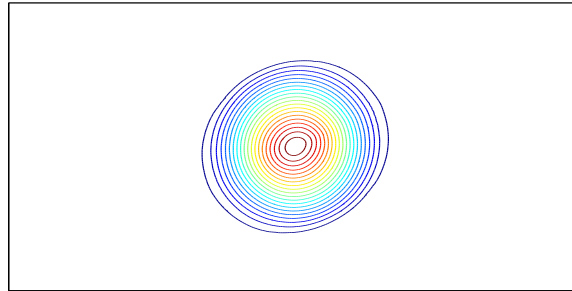


(c) Magnetic pressure at $t = 2$ without DC

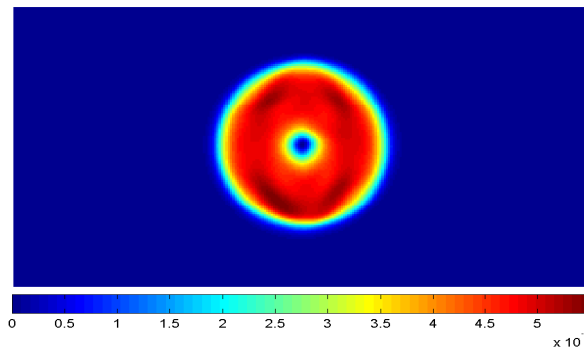
Figure 6: Effect of the DC terms on the field loop advection test.

growth of the magnetic field components. However, since the DC scheme employs the electric field value E_z from the previous time step, the dynamics of the magnetic field is coupled with the behavior of the previous time step solution. This phenomenon is seen in Figure 7(a) in that the original circular shape has evolved to an oval shape, elongated in the direction of the advection. From these tests it appears that a moderate value such as $\nu = 0.5$ is a good default choice, but a more formal analysis may be justified.

In Figure 7(b), the upwinded differencing algorithm for the MEC scheme is used. As was asserted in Section 3, the effect of upwinding the electric field does not appear to improve any qualitative behavior of the solution.



(a) Magnetic field lines at $t = 2$ with $\nu = 1$

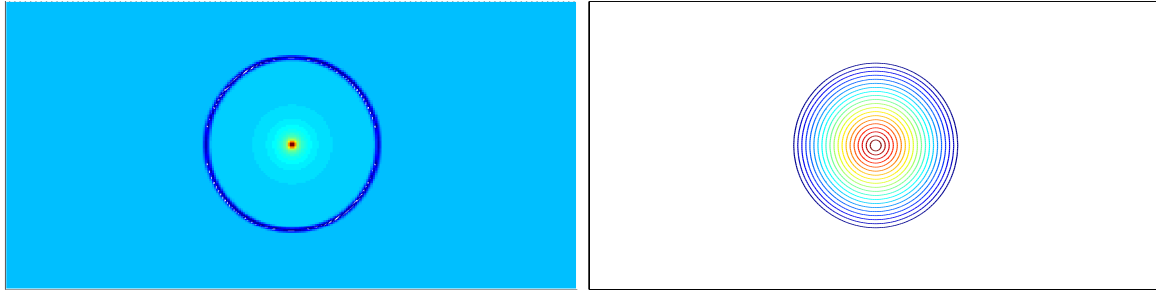


(b) Magnetic pressure at $t = 2$ using the upwinding scheme in MEC

Figure 7: A parameter test for ν is shown in (a). The larger value $\nu = 1$ tends to disrupt the circular shape of the magnetic field lines at time $t = 2$. In (b), another test using the upwinding scheme in the MEC is also illustrated.

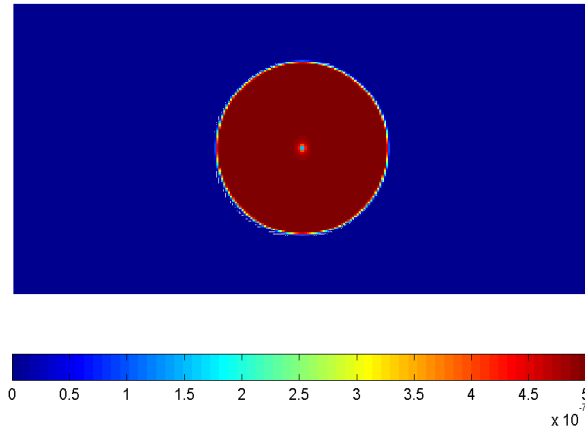
The diffusion test is now considered, where the magnetic field loop remains stationary in the domain. The only dynamics of the simulation is numerical dissipation and it diffuses the profile of the loop. In Figure 8 we observe that the USM-MEC-DC scheme maintains the circular symmetry of the flow variables by balancing terms to produce minimum possible dissipation. The small dimple in the magnetic pressure reflects the small amount of diffusion in the scheme. Indeed, the final solution in the diffusion test are almost equivalent to the initial solution, demonstrating that the USM-MEC-DC scheme works remarkably well in controlling the anti-dissipation related phenomena.

The last case in the field loop advection problem considers another diffusion case which examines in-



(a) Current density at $t = 2$

(b) Magnetic field lines at $t = 2$



(c) Magnetic pressure at $t = 2$

Figure 8: The first field loop diffusion problem on a 256×148 resolution. The solutions at time $t = 2$ are presented.

plane dynamics in two-dimensions. For two-dimensional MHD flows, it is important to maintain the relevant in-plane flow properties. To see this, we consider a variant of the previous diffusion problem, where the velocity fields are set as,

$$\mathbf{U} = (0, 0, 1). \quad (91)$$

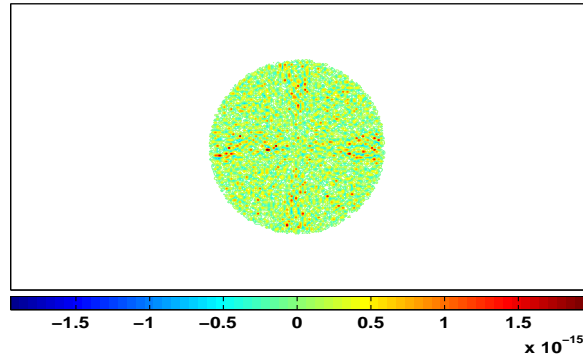
With this value, we follow how the in-plane dynamics is influenced by $\nabla \cdot \mathbf{B}$. It has been already seen in the previous diffusion test that the in-plane diffusion of the magnetic field is essentially negligible. Hence, on each subsequent time step the $\nabla \cdot \mathbf{B}$ error should be unchanged between time steps. This of course will proceed until a growth in B_z becomes sufficiently large to influence the in-plane dynamics. To see this, we examine the B_z component of the induction equation,

$$\frac{\partial B_z}{\partial t} + B_z \frac{\partial u}{\partial x} - B_x \frac{\partial w}{\partial x} - w \frac{\partial B_x}{\partial x} + u \frac{\partial B_z}{\partial x} + B_z \frac{\partial v}{\partial y} - B_y \frac{\partial w}{\partial y} - w \frac{\partial B_y}{\partial y} + v \frac{\partial B_z}{\partial y} = 0. \quad (92)$$

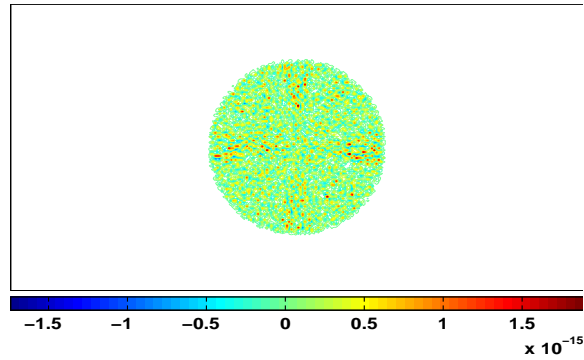
The fourth and eighth terms in the above equation (92) are the multidimensional terms that were taken care of in the data reconstruction-evolution step. The terms have been treated in an unsplit fashion using

the multidimensional characteristic method without applying any limiting (See equation (28)). The sum of these two terms is $w\nabla \cdot \mathbf{B} = w(\Delta B_{x,i}/\Delta x + \Delta B_{y,j}/\Delta y)$, and hence if there is any secular growth in the $\nabla \cdot \mathbf{B} = (\Delta B_{x,i}/\Delta x + \Delta B_{y,j}/\Delta y)$ error, it will change the in-plane geometry due to an unphysical growth of B_z with a rate proportional to $w\nabla \cdot \mathbf{B}\Delta t$. For dimensionally split MHD schemes, this kind of unphysical growth is hard to avoid, since the terms $\Delta B_{x,i}/\Delta x$ and $\Delta B_{y,j}/\Delta y$ are not updated simultaneously.

Figure 9 shows two results obtained in the USM-MEC-DC scheme at the final time step $t = 2$. The first plot (a) is the numerical values of $\nabla \cdot \mathbf{B}$ and the second plot (b) is the z component of the magnetic fields. Equally spaced 30 contour lines were plotted in both cases, and the results appear as very small amplitude noise, with values of the divergence of the magnetic fields and B_z in the range $\sim 10^{-15}$. These results show that the USM-MEC-DC scheme does indeed correctly maintain the in-plane geometry without causing an unphysical growth of the transverse field.



(a) $\nabla \cdot \mathbf{B}$



(b) B_z

Figure 9: The second diffusion problem of the field loop at $t = 2$. The numerical values of the divergence of the magnetic fields and the z component field are shown.

5.2 Circularly Polarized Alfvén Wave

The next test is the circularly polarized Alfvén wave and its propagation [17, 35]. The Alfvén wave propagates at an oblique angle to the x -axis of the computational domain. This test problem is very useful as a diagnostic of the solution's accuracy because the smooth initial conditions are nonlinear solutions to the problem. It is also of particular relevance to astrophysical phenomena because, for instance, the propagation

of Alfvén waves in the solar wind is thought to be a possible source for the heating of the solar corona. Hence their accurate modeling is crucial. Further, departures from pure Alfvénic modes are a measure of the interaction of these waves with the solar wind [18, 32].

The initial conditions we use are the same as the equivalent test problems described in [17]. A computational domain with a doubly periodic box $[0, 1/\cos\theta] \times [0, 1/\sin\theta]$ is determined according to the propagation angle θ , and the value we adopt is $\theta = \tan^{-1}(2) \approx 63.44^\circ$. In this configuration, flux terms involving $\partial B_x/\partial x$ and $\partial B_y/\partial y$ are non-zero throughout the domain and their contribution to the solution, especially the magnetic fields, are essential in this problem. For the convergence study we simulated both standing and traveling Alfvén waves.

The grid resolutions used for this problem are $2N \times N$ with $N = 4, 8, 16, 32, 64$. At time $t = 0$, the density $\rho = 1$ and the gas pressure $p = 0.1$ uniformly on the domain with $\gamma = 5/3$. The propagation of the circularly polarized Alfvén wave can be described in a rotated coordinate system using the transformation matrix T

$$\begin{pmatrix} \xi \\ \eta \\ \zeta \end{pmatrix} = \overbrace{\begin{pmatrix} \cos\theta & \sin\theta & 0 \\ -\sin\theta & \cos\theta & 0 \\ 0 & 0 & 1 \end{pmatrix}}^T \begin{pmatrix} x \\ y \\ z \end{pmatrix}, \quad (93)$$

and the analytic representation of the magnetic fields are given as

$$\mathbf{B} = (B_\xi, B_\eta, B_\zeta) = (1, 0.1 \sin 2\pi\xi, 0.1 \cos 2\pi\xi). \quad (94)$$

Similarly the velocity fields are

$$\mathbf{U} = (U_\xi, U_\eta, U_\zeta) = \begin{cases} (0, 0.1 \sin 2\pi\xi, 0.1 \cos 2\pi\xi) & \text{traveling wave,} \\ (1, 0.1 \sin 2\pi\xi, 0.1 \cos 2\pi\xi) & \text{standing wave.} \end{cases} \quad (95)$$

In both the standing and traveling cases the Alfvén wave is propagating in the ξ direction. As suggested in [17] we take numerical curls of the z -component of the magnetic vector potential A_z to assign in-plane magnetic fields, B_ξ, B_η rather than just applying T^{-1} in (93) to get analytical values of B_x, B_y . For instance, the solenoidal constraint of magnetic fields leads to,

$$\mathbf{B} = \nabla \times \mathbf{A}. \quad (96)$$

In component form for 2D,

$$\frac{\partial A_z}{\partial \xi} = -B_\eta, \quad \frac{\partial A_z}{\partial \eta} = B_\xi. \quad (97)$$

From this we integrate $B_\xi, -B_\eta$ with respect to η, ξ , respectively and sum them to get A_z . We then proceed to take numerical derivatives (e.g. central differencing) of A_z with respect to x, y to get B_x, B_y , respectively. The resulting fields are numerically divergence-free in-plane magnetic fields.

Note that in the standing wave case, the propagating Alfvén wave speed, $v_A = |B_\xi|/\sqrt{\rho}$, and the fluid velocity U_ξ are unity, and the wave moves with the flow, effectively remaining still in the computational frame.

Figure 10 shows a logarithmic scale of the numerical errors obtained with different grid resolutions. For each case the L1 error of the quantities q_k is calculated with respect to the initial condition

$$\delta q_k = \frac{1}{2N^2} \sum_i \sum_j |q_{k,i,j}^n - q_{k,i,j}^0| \quad (98)$$

by taking a sum over all cell-centered values. The errors are summed over each k -th primitive variable U_η, U_ξ, B_η and B_ξ and we compute the L1 error

$$\|\delta q\| = \sqrt{\sum_{k=1}^4 (\delta q_k)^2}. \quad (99)$$

Both the standing and traveling wave cases are evolved to $t = 5$ to obtain the final time step solutions. As shown in the figure the resulting convergence rates $\|\delta q\|$ of the USM scheme are faster than second-order accuracy N^{-2} . It is also evident that the use of the DC algorithm with $\nu = 0.5$ yields lower errors, especially in the standing wave case, where the problem is more stringent due to the larger flow velocities. This is because, as noted in [17], exact cancellations are required between the terms in the flux, for example, involving the large value $u(\partial B_y/\partial y)$ and $\partial(\nu B_x)/\partial y - B_y(\partial u/\partial y)$ for the time evolution of B_x in the induction equations. The situation is more benign in the traveling wave case because the flow velocities are much smaller. In both flows the USM scheme is seen to produce solutions that converge faster than second-order accuracy.

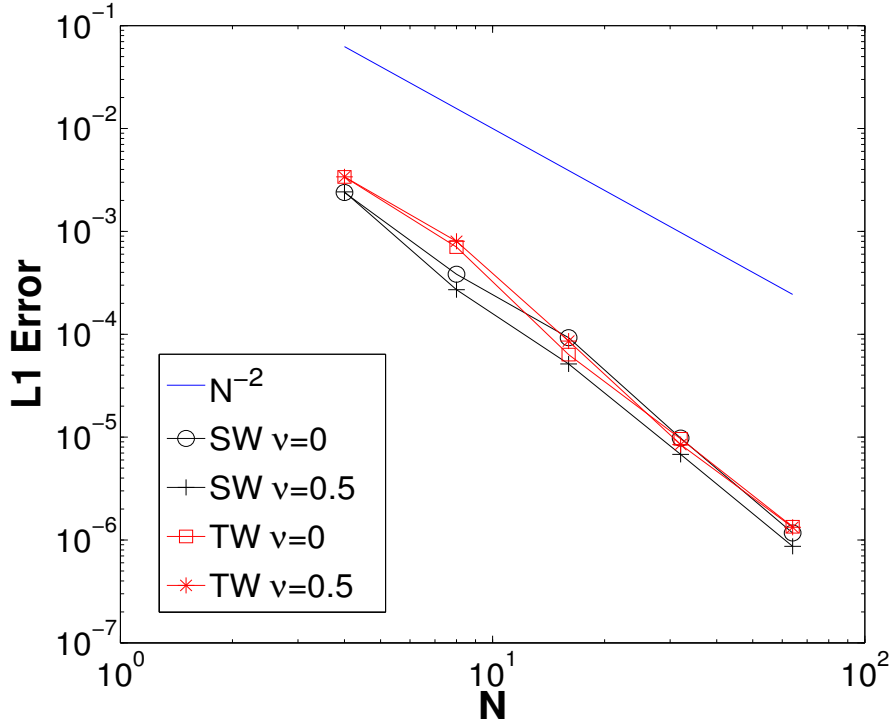


Figure 10: The circularly polarized Alfvén wave convergence rate for both the standing (labeled as SW) and traveling (labeled as TW) wave problems.

5.3 Orszag-Tang Problem

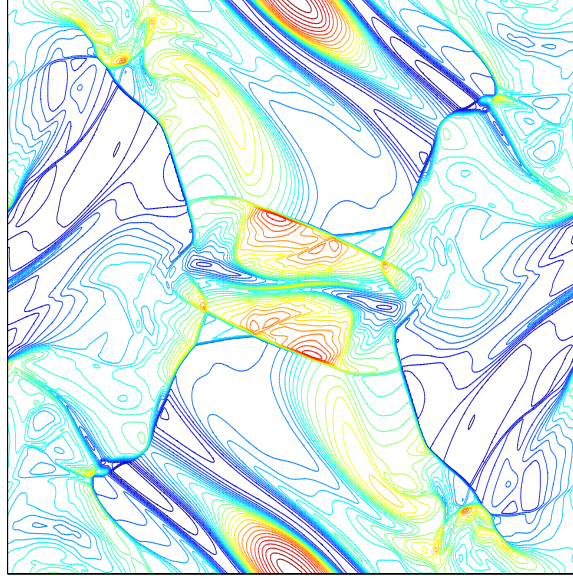
The third test problem is the Orszag-Tang MHD vortex problem [26]. This test problem is widely used in the literature and serves as a good validation test for two-dimensional MHD where nonlinear steepening builds strong discontinuities from smooth initial conditions. The computational domain is $[0, 1] \times [0, 1]$, with a resolution of $N \times N$. The initial condition is given by sinusoidal waves,

$$\mathbf{U} = u_0(-\sin\pi y, \sin 2\pi x, 0), \quad (100)$$

$$\mathbf{B} = B_0(-\sin\pi y, \sin 4\pi x, 0). \quad (101)$$

where B_0 is chosen so that the ratio of the gas pressure to the rms magnetic pressure is equal to 2γ , with $\gamma = 5/3$. The initial density, the speed of sound and u_0 are set to unity, and therefore both the initial pressure and B_0 are set to $1/\gamma$. Periodic boundary conditions are used for both boundaries. The final solutions are obtained at time $t = 0.5$.

The density contour plot on a 400×400 grid size at the final time $t = 0.5$ is shown in Figure 11. Equally spaced 30 contour lines are shown. The plot shows that the initially smooth flow has developed complicated structure involving numerous discontinuities.



(a) Density contour plot at $t = 0.5$

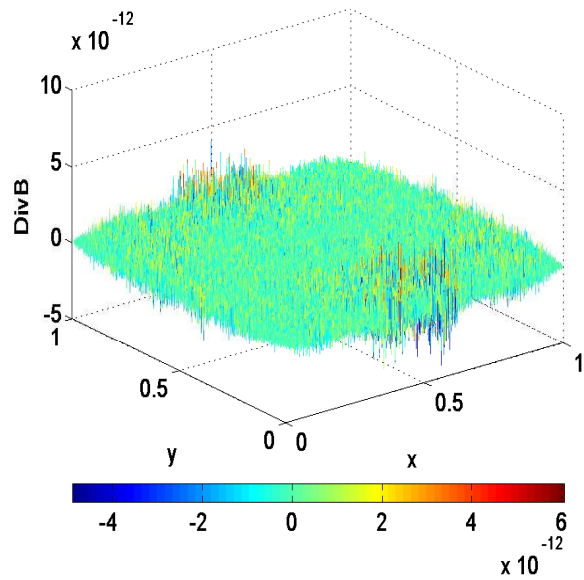
Figure 11: The density contour plot of the Orszag-Tang problem at $t = 0.5$ on a high resolution 400×400 .

Figure 12 shows two different results of $\nabla \cdot \mathbf{B}$ of numerical divergences calculated from (a) the USM-MEC-DC scheme and (b) the eight wave scheme (using the FLASH code's implementation, [16]). Clearly, very small errors in the numerical values of $\nabla \cdot \mathbf{B}$ are seen in (a), whereas the non-zero quantities are dominant in the eight wave calculation in (b). The numerical values of $\nabla \cdot \mathbf{B}$ from the eight wave calculation are shown to be quite finite (of order ~ 0.1), ranging from negative to positive. The USM-MHD scheme, however, maintains $\nabla \cdot \mathbf{B} = 0$ to about 10^{-12} over the simulation time. We can see in (b) that the non-zero values of $\nabla \cdot \mathbf{B}$ and the discontinuities of the solution are co-located implying that non-zero divergence accumulates at discontinuities.

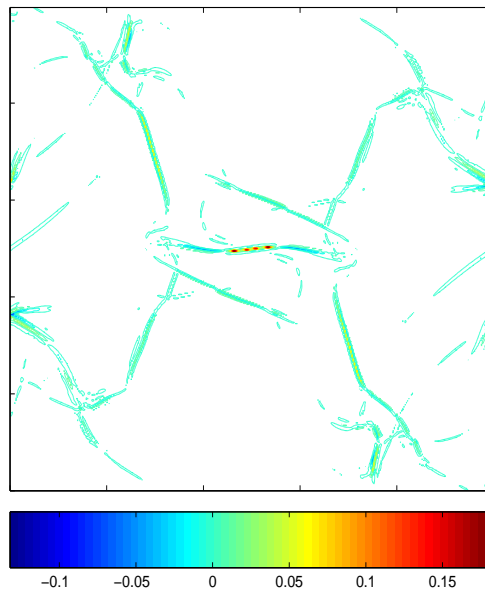
5.4 Rotor Problem

The computational domain is a unit square $[0, 1] \times [0, 1]$ with non-reflecting boundary conditions on all four sides. The initial conditions are given by

$$\rho(x, y, 0) = \begin{cases} 10 & \text{for } r \leq r_0 \\ 1 + 9f(r) & \text{for } r_0 < r < r_1 \\ 1 & \text{for } r \geq r_1 \end{cases} \quad (102)$$



(a) $\nabla \cdot \mathbf{B}$ of USM-MEC-DC scheme.



(b) $\nabla \cdot \mathbf{B}$ of eight wave scheme.

Figure 12: The divergence-free properties obtained from the (a) USM-MEC-DC scheme and (b) eight wave scheme.

$$u(x,y,0) = \begin{cases} -f(r)u_0(y-0.5)/r_0 & \text{for } r \leq r_0 \\ -f(r)u_0(y-0.5)/r & \text{for } r_0 < r < r_1 \\ 0 & \text{for } r \geq r_1 \end{cases} \quad (103)$$

$$v(x,y,0) = \begin{cases} f(r)u_0(x-0.5)/r_0 & \text{for } r \leq r_0 \\ f(r)u_0(x-0.5)/r & \text{for } r_0 < r < r_1 \\ 0 & \text{for } r \geq r_1 \end{cases} \quad (104)$$

$$p(x,y,0) = 1 \quad (105)$$

$$B_x(x,y,0) = \frac{5}{\sqrt{4\pi}} \quad (106)$$

$$B_y(x,y,0) = 0, \quad (107)$$

where $r_0 = 0.1, r_1 = 0.115, r = \sqrt{(x-0.5)^2 + (y-0.5)^2}, w = B_z = 0$ and a taper function $f(r) = (r_1 - r)/(r - r_0)$. The value $\gamma = 1.4$ is used. The initial set-up is therefore occupied by a dense rotating disk at the center of the domain, surrounded by ambient gas at rest with uniform density and pressure. The rapidly spinning rotor is not in an equilibrium state due to centrifugal forces. As the rotor spins with the given rotating velocity, the initially uniform magnetic field in x -direction winds up the rotor. The magnetic field wraps around the rotor, and subsequently launches torsional Alfvén waves into the ambient gas. The angular momentum of the rotor is diminished at later times. The circular rotor is progressively compressed into an oval shape by the build-up of the magnetic pressure around the rotor.

Shown in Figure 13 are the contour plots of (a) the density, (b) the gas pressure, (c) the Mach number and (d) the magnetic pressure at the final time $t = 0.15$ on a grid resolution 400×400 . For all cases (a)-(d), 30 equally spaced contour lines are plotted. By this final time, we can see in (d) that the Alfvén waves have almost reached the boundary. One of the important features of this rotor test problem is the maintenance of smooth contour profiles in the central part of the Mach number profile[35]. A scheme that produces undershoots in pressure and correspondingly the sound speed, will result in spurious peaks in the Mach number field, especially in the central region. A distortion of the oval contour lines is a signature of a relatively poor performance of a scheme. The USM-MEC-DC scheme shows excellent behavior as illustrated in (c) where such distortions are absent and the rotor possesses smooth contours.

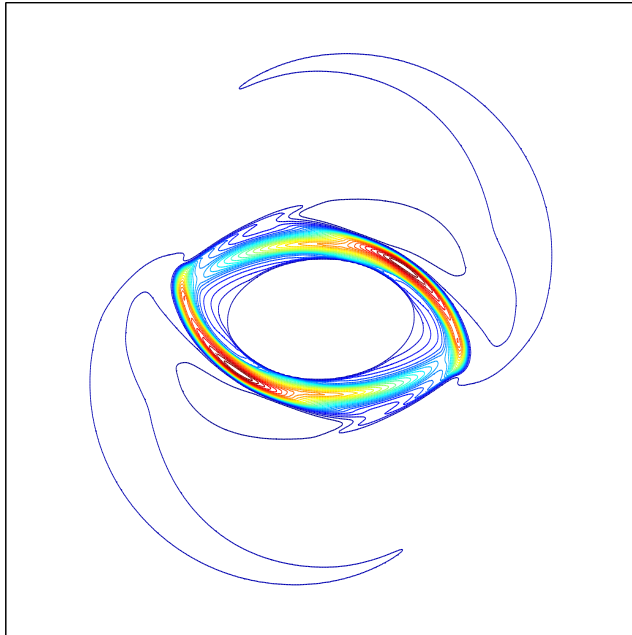
For a comparison at the lower resolution used in Tóth [35], the Mach number on a 100×100 resolution is computed and shown in Figure 14. In Figure 20 of [35], seven different Mach number plots were obtained from seven different MHD schemes at the same resolution of (100×100) and compared. Those results can be compared with plot (b) of Figure 14 showing results of the present scheme. The results of the USM-MEC-DC scheme appear to be among best of the results presented in [35], indicating that the present scheme is more accurate and reliable than many of the other conventional MHD schemes.

In the work of Londrillo & Del Zanna [24], a similar rotor problem was presented with minor changes in the flow parameters. While their results appear convincing, the divergence of the magnetic fields as shown reaches values up to the order of 10^{-4} on their 240×240 resolution calculation. The USM-MEC-DC scheme, however, keeps this value to the order of 10^{-12} (even with a lower resolution of size 200×200).

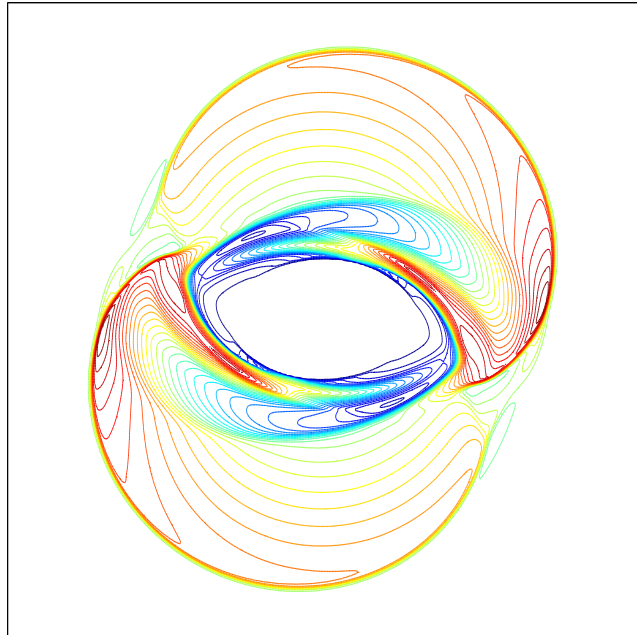
5.5 Cloud & Shock Interaction

The next test problem considers the interaction of a high density cloud with a strong shock wave. This problem, also known as the Dai & Woodward's cloud-shock problem [12], has been studied in several papers [23,35] to test the robustness of MHD schemes. The challenge for this problem is to demonstrate supersonic flow in the pre-shock and the post-shock regions, as well as the correct physics near the sharp boundary of the cloud.

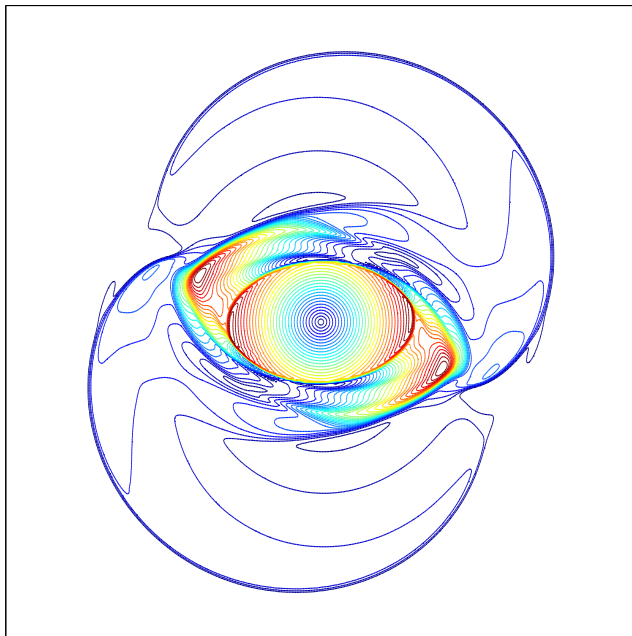
The same initial condition is adopted as presented in [35]. The flow is solved on the computational domain of size $[0, 1] \times [0, 1]$ on a uniform $N \times N$ grid. The simulation is carried out to the final time $t = 0.06$



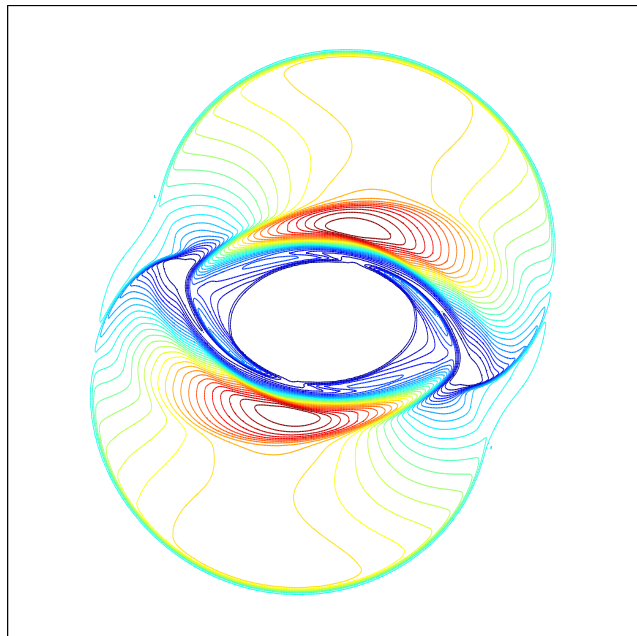
(a) Density at $t = 0.15$



(b) Gas pressure at $t = 0.15$

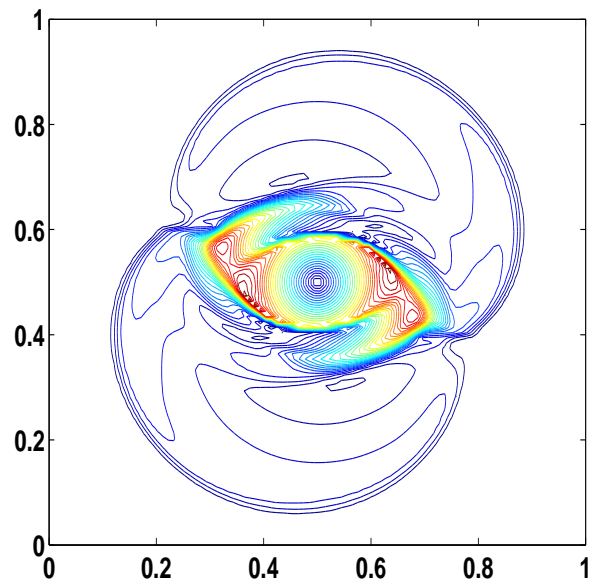


(c) Mach number at $t = 0.15$

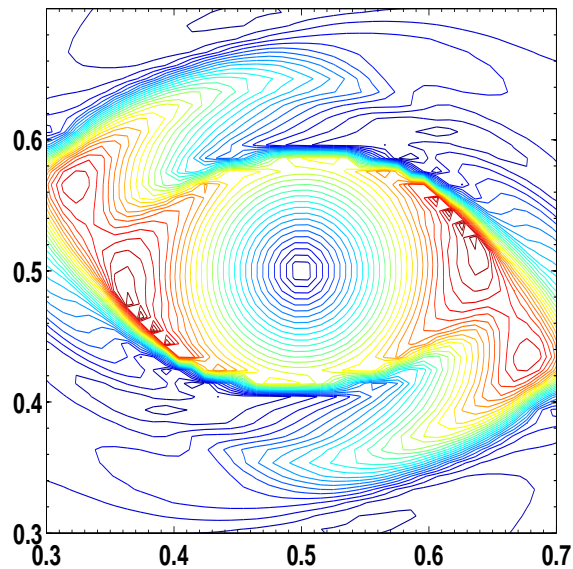


(d) Magnetic pressure at $t = 0.15$

Figure 13: The rotor problem on a resolution of 400×400 . Thirty equally spaced contour lines are plotted.



(a) Mach number at $t = 0.15$



(b) A close up view at the center

Figure 14: The Mach number for the rotor problem on a resolution of 100×100 . Thirty equally spaced contour lines are plotted. In (b) the circular shapes of the contour lines are well captured even with this low resolution.

with $N = 400$. The initial discontinuity involves the left and right states along a line $x = 0.6$ parallel to the y axis, with

$$(\rho, u, v, w, B_x, B_y, B_z, p) = \begin{cases} (3.86859, 0, 0, 0, 0, 2.1826182, -2.1826182, 167.345) \\ \text{if } x \leq 0.6, \\ (1, -11.2536, 0, 0, 0, 0.56418958, 0.56418958, 1) \\ \text{if } x > 0.6. \end{cases} \quad (108)$$

The high density cloud is located on the right side of the domain, for which its circular shape is defined by $(x - 0.8)^2 + (y - 0.5)^2 = 0.15^2$. Uniform density $\rho = 10$ and the pressure $p = 1$ are fixed in the inner region, and $\gamma = 5/3$. The velocity and the magnetic fields are the same as the surrounding right state plasma values. Supersonic inflow boundary conditions are imposed along the right-most boundary at $x = 1$ and outflow boundary conditions are used for all other boundaries.

As shown in the density plots in Figure 15, the temporal evolution involves the disruption of the high density cloud by the shock initially located at $x = 0.6$. The light areas indicate the strongly shocked regions and compare well with the results in [23, 35]. It was found by Tóth that a simple dimensionally split MHD algorithm can easily fail due to unphysical states (e.g., negative pressure or density) produced during the strong interaction of the shock with the cloud even when the rather diffusive MINMOD limiter was used. In the USM-MEC-DC scheme, the final time step is reached successfully without such problems.

5.6 MHD Blast Wave

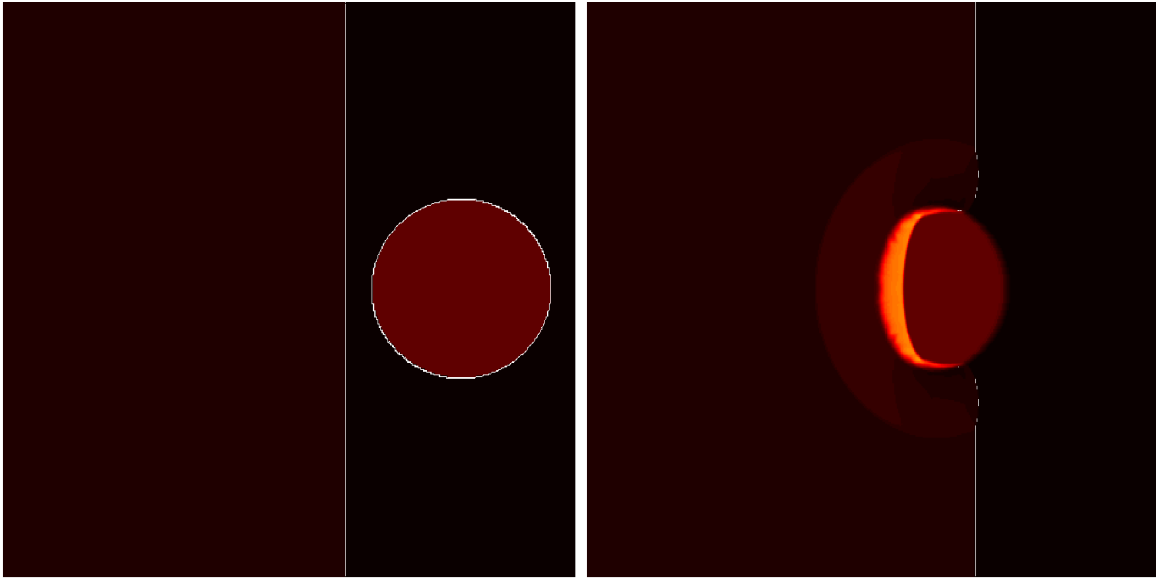
The last test case presented is the MHD spherical blast wave problem of Zachary *et al.* [37]. This problem leads to the formation and propagation of strong MHD discontinuities, relevant to astrophysical phenomena where the magnetic field energy has strong dynamical effects. With a numerical scheme that fails to preserve the divergence-free constraint, unphysical states can be obtained involving negative gas pressure because the background magnetic pressure increases the strength of magnetic monopoles.

This problem was computed in two different flow regimes by taking intermediate and strong magnetic field strengths. The computational domain is a square $[-0.5, 0.5] \times [-0.5, 0.5]$ with a grid of resolution 200×200 . The explosion is driven by an over-pressurized circular region at the center of the domain with a radius $r = 0.1$. The initial density is unity everywhere. The pressure of the ambient gas is 0.1, while the pressure of the inner region is 1000. Two different regimes of a uniform magnetic field in the x -direction are studied, with $B_x = 50/\sqrt{4\pi}$ and $100/\sqrt{4\pi}$. These initial conditions result in very low- β ambient plasma states, $\beta = 1 \times 10^{-3}$ and 2.513×10^{-4} respectively. Through these low- β ambient states, the explosion emits almost spherical fast magneto-sonic shocks that propagate with the fastest wave speed. The flow has $\gamma = 1.4$.

The intermediate magnetic field strength case with $B_x = 50/\sqrt{4\pi}$ is illustrated in Figure 16. We see an anisotropic explosion behavior because of the existence of the non-zero magnetic field strength in x -direction. With this value of the B_x field, the shock waves still somewhat preserve the spherically symmetric shapes, although the development of the elongated wave structures in the direction parallel to the B_x field are evident.

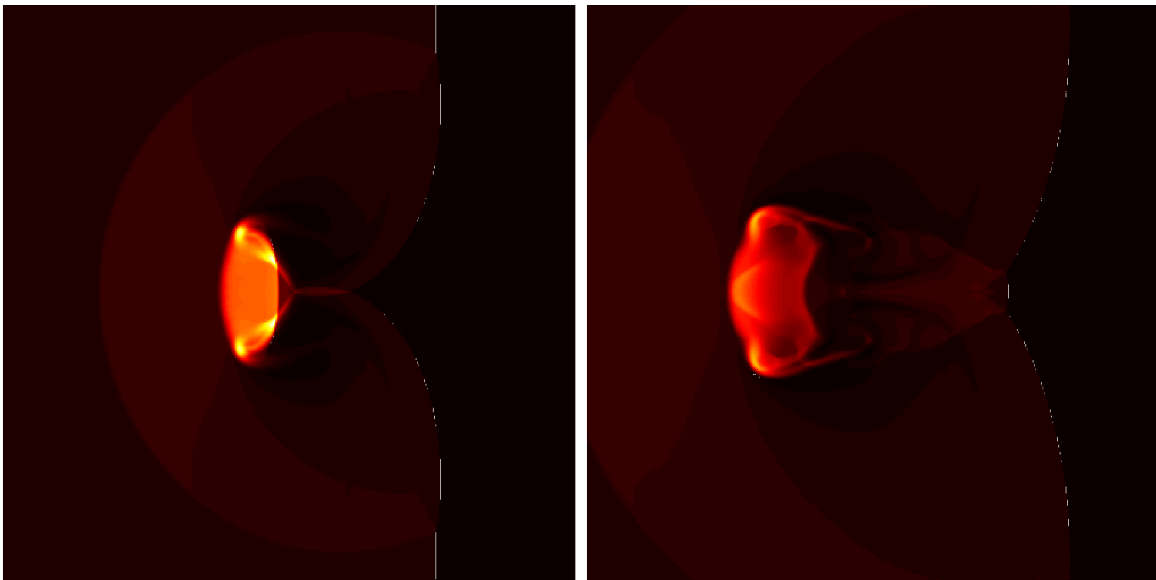
For a stronger magnetic field strength $B_x = 100/\sqrt{4\pi}$, shown in Figure 17, the explosion now becomes highly anisotropic. In Figure 17(b), the displacement of gas in the transversal y -direction is increasingly inhibited and hydrodynamical shocks propagate in both positive and negative x -directions parallel to B_x . It is also evident in (d) that several weak magneto-sonic waves are radiated transverse to x -direction. This process continues until total pressure equilibrium is reached in the central region.

Balsara [4] found that the strong wave propagation oblique to the mesh can cause unphysical negativity in the pressure. Such effects are manifested as distortions of contours especially near the outer boundary, where a large and unphysical drop in pressure takes place immediately ahead of the shock. No such excrescence is evident in our calculation.



(a) Density at $t = 0.0$

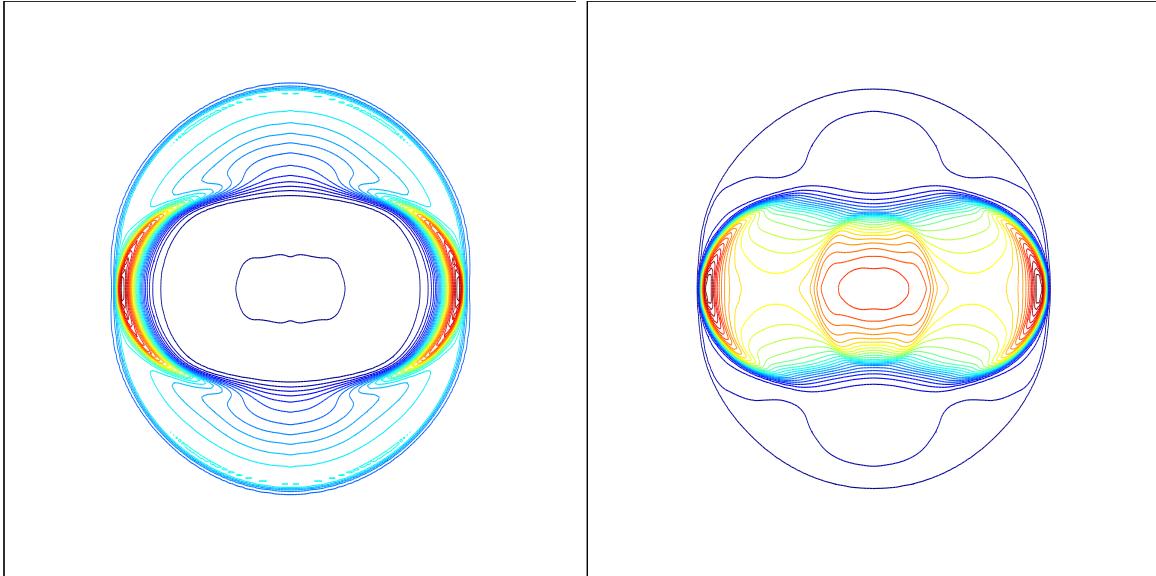
(b) Density at $t = 0.02$



(c) Density at $t = 0.04$

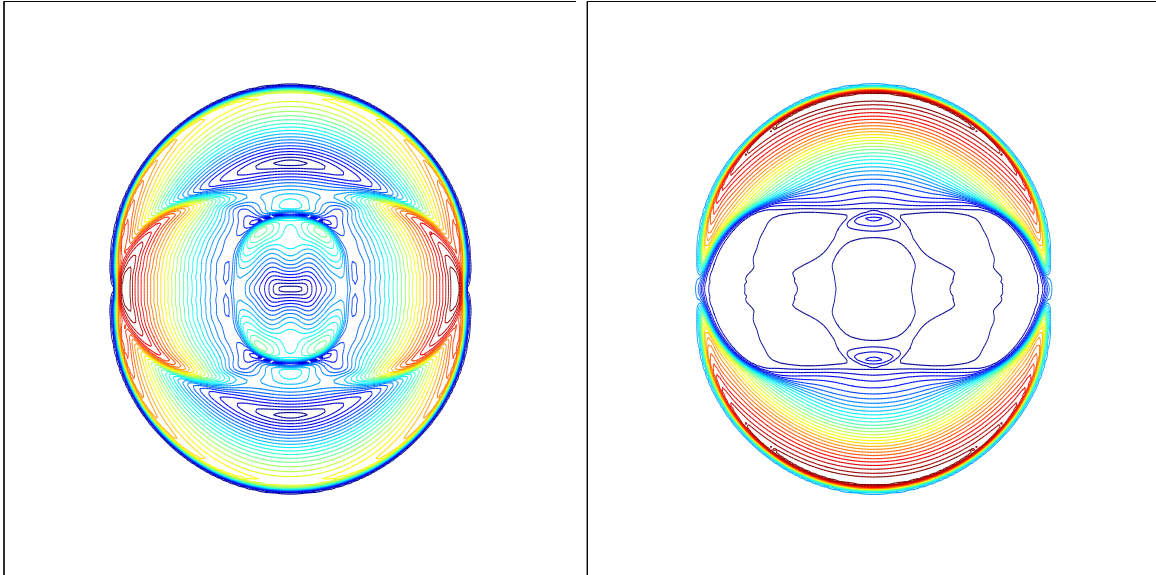
(d) Density at $t = 0.06$

Figure 15: The MHD interaction between the high density cloud and shock structures resolved on 400×400 grid. All plots show in a same color scheme ranging between 0.6599 (*dark*) and 70.7662 (*bright*).



(a) Density at $t = 0.01$

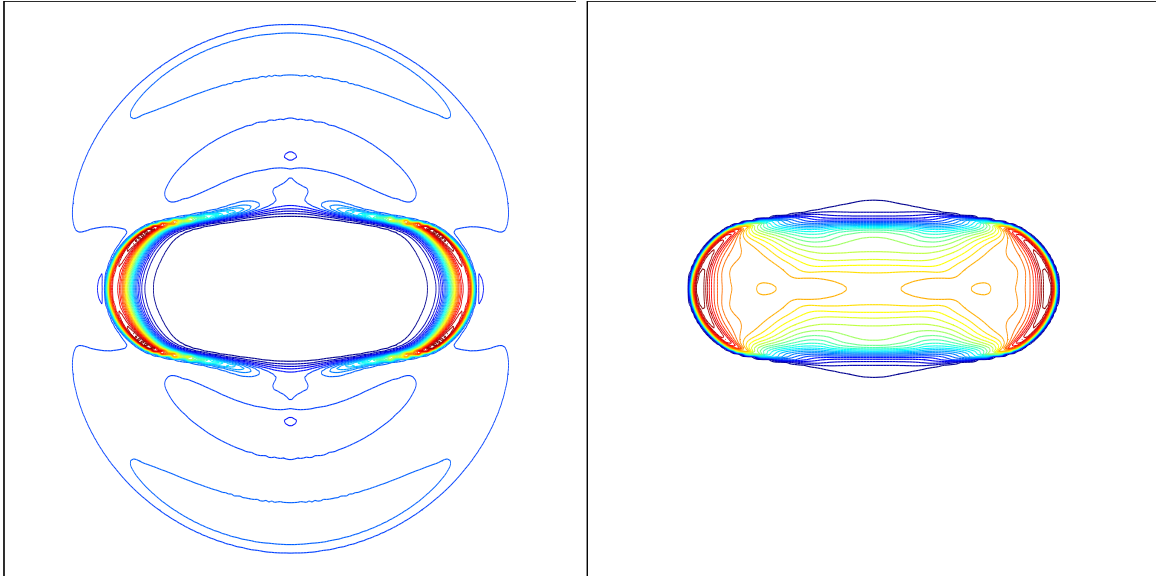
(b) Gas pressure at $t = 0.01$



(c) Total velocity $|U|$ at $t = 0.01$

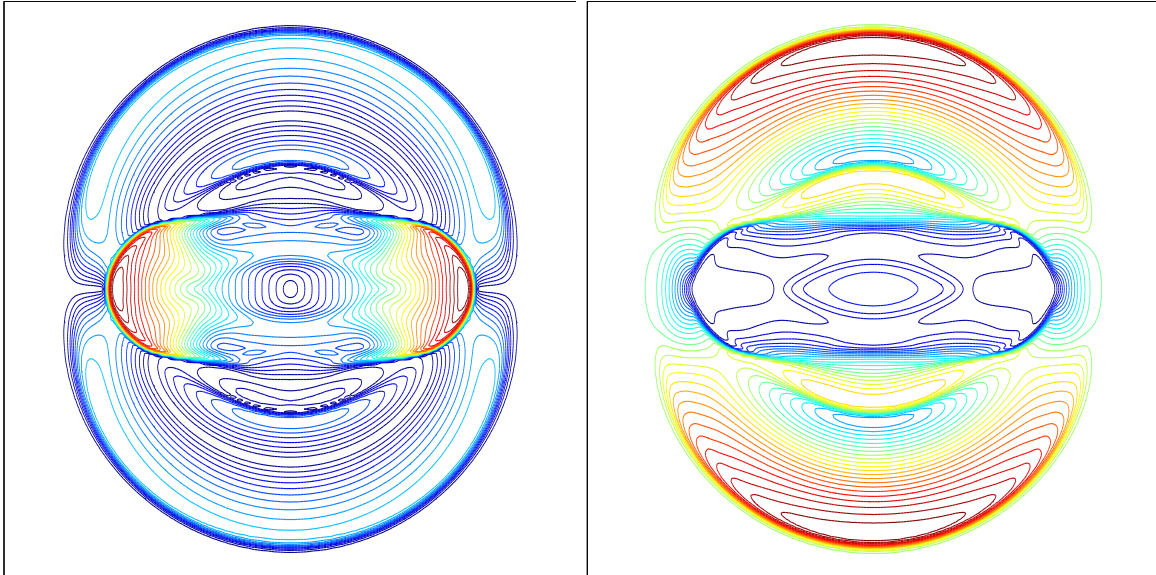
(d) Magnetic pressure at $t = 0.01$

Figure 16: Results from the blast problem with $B_x = 50/\sqrt{4\pi}$.



(a) Density at $t = 0.01$

(b) Gas pressure at $t = 0.01$



(c) Total velocity $|U|$ at $t = 0.01$

(d) Magnetic pressure at $t = 0.01$

Figure 17: Results from the blast problem with $B_x = 100/\sqrt{4\pi}$.

We further consider the possibility of an unphysical drop in pressure by looking at this field on a logarithmic scale. It is asserted in [4] the scheme presented there (a modified flux-CT scheme with slope limiters, denoted as the fast TVD limiter and a multidimensional limiter) performs well for this stringent blast problem, and indeed it is stable and able to capture the main features of the flow. However, as published in Figures 6(b,f) of [4], drops in the pressure can be observed particularly in regions where the direction of the strong wave propagation is oblique to the mesh. In their 6(b), with the fast TVD slope limiter employed, distorted profiles at the outer boundary in these regions are evident, while in their 6(f) these effects are seen to be mitigated but not eliminated with the use of the multidimensional slope limiter. In contrast, as shown in Figure 18, the USM-MEC-DC scheme displays sharper profiles in these regions at the outer boundary. The modified flux-CT scheme in [4] appears more diffusive than the present scheme and exhibits a narrower bandwidth in the y direction at the center of the inner blast wave structure. It also appears that the overall wave structures are predicted in more detail with the USM-MEC-DC scheme, while regions appear featureless with the modified flux-CT scheme with slope limiters scheme of [4], although this could be a plotting artifact of the latter figures. The dissipation control from the DC scheme also produces sharper features in the pre-shock regions in both the negative and positive x -axis directions, while the figures in Figures 6(b,f) of [4] display more diffuse features.

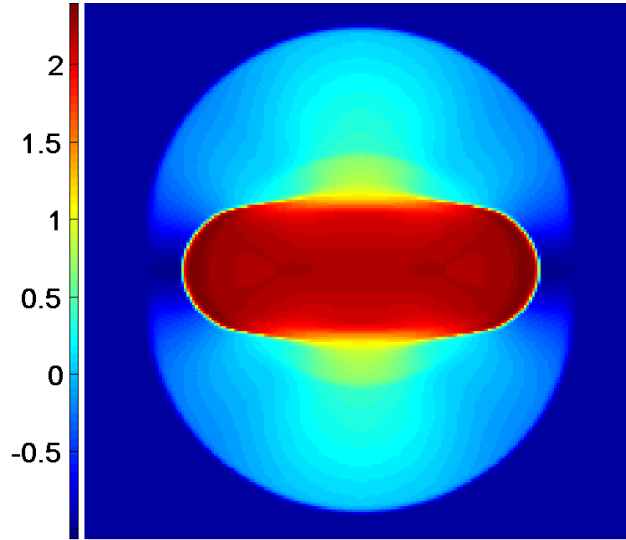


Figure 18: Shown is $\log_{10} p$ at $t = 0.01$ for the blast problem with $B_x = 100/\sqrt{4\pi}$ for the USM-MEC-DC scheme.

The test case shows that the USM-MEC-DC scheme does not suffer from observable unphysical effects in strongly shocked cases and continues to maintain sharp features. The results are found compare quite favorably in comparison with other MHD schemes which can generate the strong distortions of the outer contours (See [22]). For instance, Figure 17 of [22]) shows the contour plot of the density using the eight wave scheme, where numerous unphysical peaks and distortions are evident in the contours. In contrast, smooth contours mark the density field in the USM-MEC-DC calculation shown in Figure 17(a).

Several other CT-type schemes were tested in [22], including the modified flux-CT of [4] and upwinding-CT (UTC) schemes. The study points out that the negativity of the pressure variable could easily be introduced, especially in low- β simulations like the blast wave problem, and found it useful to turn on an energy-fix switch in order to overcome the issue. The situation was found to be more severe in the UTC-based schemes in that some specific parameters were needed in many cases for successful completion of the calculation.

While ameliorating the pressure negativity issue, there still exist other distortions of the fields using

these schemes as indicated in Figure 19 of [22]). It can also be seen in plots of their so-labeled BS2 and BS3 that, as mentioned earlier, there appears to be no qualitative difference between the results when adopting the comparatively newer reconstruction scheme of [4], equations (86) and (87).

6 Conclusion

The USM-MEC-DC scheme has been introduced, developed and studied in this paper. The method uses characteristic analysis to account for the contribution of both normal and transversal MHD fluxes. A modified electric field construction (MEC) scheme and a new, very efficient, dissipation control algorithm (DC) has been presented. The results of several test problems presented give considerable confidence in the scheme for use as a robust and reliable second-order MHD algorithm.

The second-order accurate, multidimensional, unsplit high-order Godunov MHD algorithm has been successfully developed on a staggered grid, with the capability of maintaining divergence-free magnetic fields numerically. The method preserves the constraint numerically extremely well without evidence of numerical instability or accumulation of unphysical errors. As validation, the suite of test problems presented in this study include several stringent setups that stress various features of MHD algorithms. They consist of the evolution of a very weak magnetic field loop, a convergence study of circularly polarized Alfvén waves, the widely used benchmark Orszag-Tang vortex problem, the spinning rotor problem, magnetic cloud-shock interaction, and the MHD blast wave problem. The scheme has been thoroughly tested and has been shown to perform very well, providing confidence in correctly simulating a wide range of MHD physical phenomena.

The scheme handles multidimensional MHD terms consistently using the characteristic method. Such multidimensional treatment has been ignored in many of the operator splitting based MHD schemes. The approach involves physical considerations that multidimensional MHD schemes should manifest. In particular, such multidimensional considerations eliminate unphysical secular growth that would cause deviations from the in-plane dynamical evolution. To ascertain this, a two-dimensional MHD problem of field loop diffusion was computed. Spurious numerical errors proportional to $\nabla \cdot \mathbf{B}$ would affect the growth of B_z , and ultimately alter the in-plane dynamics of the problem. These were found to be absent. The presented data reconstruction-evolution method resolves the issue by using the multidimensional characteristic method in a straightforward way.

A new procedure has been developed to construct the electric field in the MEC scheme, which appears to significantly improve the accuracy of similar schemes (e.g., the flux-CT scheme of Reference [2]). The MEC scheme takes a more directional consideration of the high-order Godunov fluxes obtained from the duality relationship in the flux-CT scheme.

Remarkably good results are found with the introduction and development of the DC scheme for the induction equation, in that a significant improvement in the solution of magnetic fields is found, which is particularly observable in the field loop tests. We find that for our scheme, without utilizing the DC scheme for the simulation, the circular symmetry of the field loop is destroyed. A balancing of the numerical dissipation in MHD schemes is found to be important not only for the accuracy of solutions, but even for stability. The DC scheme provides insight into suppressing undesirable anti-dissipative effects that potentially exist in the solving the induction equation.

This paper has detailed the core algorithmic features of the USM-MEC-DC scheme, laying down the important multidimensional aspects, and subjecting it to a series of tests. In subsequent publications we will present extensions of this scheme that support parallel adaptive mesh refinement (early parallel results were reported in [21]) and implementation in fully three dimensions.

The scheme has been implemented and is currently available in the University of Chicago ASC FLASH Center’s FLASH 3 release [16].

7 Acknowledgments

This work has been supported in part by National Science Foundation ITR grant DMS-0219282. The FLASH code has been developed by the DOE-supported ASC/Alliance Center for Astrophysical Thermonuclear Flashes at the University of Chicago. This work is supported by the U.S. Department of Energy under Grant No. B523820 to the Center for Astrophysical Thermonuclear Flashes at the University of Chicago. The first author gratefully acknowledge the FLASH code group for help and for supporting the current work. The authors would like to thank Dr. James Stone at Princeton University and Dr. Timur Linde, previously at the FLASH center and now in industry, for useful discussions and comments on an early work of this paper. We also acknowledge useful discussions with Dr. Robert Fisher at the FLASH center, University of Chicago. The authors especially thank Dr. Kevin Olson at the Drexel University for helpful support during the course of this work.

References

- 1 Balsara, D. S., Total Variation Diminishing Scheme for Adiabatic and Isothermal Magnetohydrodynamics, *Astrophys. J. Suppl.*, 116:133–153, 1998.
- 2 Balsara, D. S., Spicer, D. S., A Staggered Mesh Algorithm Using High Order Godunov Fluxes to Ensure Solenoidal Magnetic Fields in Magnetohydrodynamics Simulation, *J. Comput. Phys.*, 149:270–292, 1999.
- 3 Balsara, D. S., Divergence-Free Adaptive Mesh Refinement for Magnetohydrodynamics, *J. Comput. Phys.*, 174:614–648, 2001.
- 4 Balsara, D. S., Second-Order-Accurate Schemes For Magnetohydrodynamics With Divergence-Free Reconstruction, *Astrophys. J. Suppl.*, 151:149–184, 2004.
- 5 Balsara, D. S., Kim, D., An Intercomparison Between Divergence-Cleaning and Staggered Mesh Formulations for Numerical Magnetohydrodynamics, *Astrophys. J.*, 602:1079-1090, 2004 February 20 2004.
- 6 Brackbill, J. U., Barnes, D. C., The Effect of Nonzero $\nabla \cdot \mathbf{B}$ on the Numerical Solution of the Magnetohydrodynamic Equations, *J. Comput. Phys.*, 87:171–200, 1990.
- 7 Brecht, S. H., Lyon, J. G., Fedder, J. A., Hain, K., *Geophys. Res. Lett.*, 8:397, 1981.
- 8 Brio, M., Wu, C. C., An Upwind Differencing Scheme for the Equations of Ideal Magnetohydrodynamics, *J. Comput. Phys.*, 75:400–422, 1988.
- 9 Colella, P., Multidimensional Upwind Methods for Hyperbolic Conservation Laws, *J. Comput. Phys.*, 87:171–200, 1990.
- 10 Crockett, R. K., Colella, P., Fisher, R. T., Klein, R. I., McKee, C. F., An Unsplit, Cell-Centered Godunov Method for Ideal MHD, *J. Comput. Phys.*, 203:422–448, 2005.
- 11 Dai, W., Woodward, P., An Approximate Riemann Solver for Ideal Magnetohydrodynamics, *J. Comput. Phys.*, 111:354–372, 1994.
- 12 Dai, W., Woodward, P., A Simple Finite Difference Scheme for Multidimensional Magnetohydrodynamics, *J. Comput. Phys.*, 142:331–369, 1998.

- 13 Dedner, A., Kemm, F., Kröner, D., Munz, C. D., Schnitzer, T., Wesenberg, M., Hyperbolic Divergence Cleaning for the MHD Equations, *J. Comput. Phys.*, 175:645–673, 2002.
- 14 DeVore, C. R., Flux Corrected Transport Techniques for Multidimensional Compressible Magnetohydrodynamics, *J. Comput. Phys.*, 92:142, 1991.
- 15 Evans, C. R., Hawley, J. F., Simulation of Magnetohydrodynamic Flows: A Constrained Transport Method, *Astrophys. J.*, 332:659–677, 1988.
- 16 FLASH, <<http://flash.uchicago.edu>>, 2007.
- 17 Gardiner, T., Stone, J., An Unsplit Godunov Method for Ideal MHD via Constrained Transport, *J. Comput. Phys.*, 205:509–539, 2005.
- 18 Goldstein, M. L., Roberts, D. A., Deane, A. E., Ghosh, S., Numerical Simulation of Alfvénic Turbulence in the Solar Wind, *J. Geophys. Res.*, 104, A7:14437–14451, 1999.
- 19 Goldstein, M. L., Roberts, D. A., Burlaga, L. F., Sirigar, E., Deane, A. E., North-south flows observed in the outer heliosphere at solar minimum: Vortex streets or corotating interaction regions?, *J. Geophys. Res.*, 106, A8:15973–15984, 2001.
- 20 Janhunen, P., A Positive Conservative Method for Magnetohydrodynamics Based on HLL and Roe Methods, *J. Comput. Phys.*, 160:649, 2000.
- 21 Lee, D., Deane, A., A Parallel Unsplit Staggered Mesh Algorithm for Magnetohydrodynamics, Parallel CFD, Egmond En Zee, Netherlands, 2005.
- 22 Li, S., Note on Upwinding Constrained Transport Method for Ideal Magnetohydrodynamics, *Los Alamos Report*, LA-UR-03-8925, 2003.
- 23 Li, S., Li, H., A Modern Code for Magneto-hydrodynamics or Hydrodynamics Equations, *Los Alamos Report*, LA-UR-03-8925, 2003.
- 24 Londrillo, P., Del Zanna, L., High Order Upwind Schemes For Multidimensional Magnetohydrodynamics, *Astrophys. J.*, 530:508–524, 2000.
- 25 Londrillo, P., Del Zanna, L., On the Divergence-Free Condition in Godunov-Type Schemes for Ideal Magnetohydrodynamics: The Upwind Constrained Transport Method, *J. Comput. Phys.*, 195:14–48, 2004.
- 26 Orszag, A., Tang, C. M., Small-scale Structure of Two-Dimensional Magnetohydrodynamics Turbulence, *J. Fluid Mech.*, 90:129–143, 1979.
- 27 Pen, U., Arras, P., Wong, S., A Free, Fast, Simple and Efficient TVD MHD Code, *Astrophys. J. Suppl.*, 149:447–455, 2003.
- 28 Powell, K. G., A Riemann Solver for Ideal MHD: That works in More Than One Dimension, ICASE Report, 94–24, Langely, VA, 1994.
- 29 Powell, K. G., Roe, P. L., Linde, T. J., Gombosi, T. I., De Zeeuw, D. L., A Solution-Adaptive Upwind Scheme for Ideal Magnetohydrodynamics, *J. Comput. Phys.*, 154:284–309, 1999.
- 30 Ryu, D., Jones, T. W., Numerical Magnetohydrodynamics in Astrophysics: Algorithm and Tests for One-dimensional Flow, *Astrophys. J.*, 442:228–258, 1995.

- 31 Ryu, D, Miniati, F., Jones, T. W., Frank, A., A Divergence-Free Upwind Code For Multidimensional Magnetohydrodynamic Flow, *Astrophys. J.*, 509:244–255, 1999.
- 32 Ruderman, M. S., Goldstein, M. L., Roberts, D. A., Deane, A. E., Ofman, L., Alfvén wave phase mixing driven by velocity shear in two-dimensional open magnetic configurations, *J. Geophys. Res.*, 104, A8:17057–17068, 1999.
- 33 Stone, J., The Athena Test Suite, <<http://www.astro.princeton.edu/~jstone>>
- 34 Toro, E. F., *Riemann Solvers and Numerical Methods for Fluid Dynamics, A Practical Introduction*, Springer, 1997.
- 35 Tóth, G., The $\nabla \cdot \mathbf{B} = 0$ Constraint in Shock-Capturing Magnetohydrodynamics Codes, *J. Comput. Phys.*, 161:605–656, 2000.
- 36 Yee, K. S. Numerical Solution of Initial Boundary Value Problems Involving Maxwell’s Equations in Isotropic Media *IEEE Trans. Antenna Propagation*, AP-14:302–307
- 37 Zachary, A., Malagoli, A., Colella, P., A Higher-Order Godunov Method for Multidimensional Ideal Magnetohydrodynamics, *J. Comput. Phys.*, 2:263–284, 1994.